Title: Top-Down Benchmark of U.S. Methane Inventories Reveals Regional Discrepancies in Activity-Based Estimates

Authors: John Worden[1,2,*], Sudhanshu Pandey[1,*], Hannah Nesser[1], Kevin Bowman[1], Colin Harkins[4,8], Congmeng Lyu[4,8], Joannes D. Maasakkers[5], Deborah Gordon[6], Daniel Jacob[3], Lucas Estrada[3], Daniel J. Varon[9,3], James D. East[3], Lauren Schmeisser[6,] and Zhen Qu[7]

1. Jet Propulsion Laboratory, California Institute of Technology, Pasadena, California, United States
2. Joint Institute for Regional Earth System Science and Engineering, University of California, Los Angeles, Los Angeles, California, United States
3. Harvard University, Cambridge, Massachusetts, United States
4. NOAA Chemical Sciences Laboratory, Boulder, Colorado, United States
5. SRON Netherlands Institute for Space Research, Leiden, The Netherlands
6. Rocky Mountain Institute, Boulder, Colorado, United States
7. North Carolina State University, Raleigh, North Carolina, United States
8. Cooperative Institute for Research in Environmental Sciences, University of Colorado Boulder, Boulder, Colorado, United States
9. Massachusetts Institute of Technology, Cambridge, Massachusetts, United States

[*]These authors contributed equally to the work.

[*] Correspondence to: John Worden jworden@g.ucla.edu

Abstract: Robust estimates of methane emissions are critical for understanding their impacts on atmospheric warming and air quality, and for assessing methane mitigation strategies. Gridded inventories, such as the U.S. Environmental Protection Agency's Greenhouse Gas Inventory (EPA GHGI), the Emissions Database for Global Atmospheric Research (EDGAR 2024), and the National Oceanic and Atmospheric Administration's Fossil Fuel Oil and Gas inventory (NOAA FOG), are constructed to evaluate large-scale emission patterns and support identifying emission mitigation priorities and prioritizing future measurements. However, substantial differences across inventories complicate such assessments. We benchmark EPA GHGI, EDGAR 2024, and NOAA FOG against flux estimates from an atmospheric inversion of Greenhouse Gases Observing Satellite (GOSAT) data from 2012 to 2020 over the Contiguous United States (CONUS). A key technical challenge is the heterogeneous sensitivity of satellite-derived fluxes, which depends on measurement uncertainty, coverage, and inversion model configuration. We account for this heterogeneity by applying an inversion operator to each

inventory prior to comparison with the GOSAT-based estimates. The GOSAT estimates are most sensitive to oil&gas and livestock emissions; oil and gas emissions are consistent with NOAA FOG (14.1 Tg CH_4 yr^{-1} in 2015), but exceed EPA GHGI and EDGAR, particularly across Texas, Oklahoma, and Louisiana. GOSAT-based livestock emissions exceed EPA GHGI and EDGAR by 1–2 Tg CH_4 yr^{-1}, with the largest differences in the Midwest and California. Despite these discrepancies, both activity and satellite based estimates show no observable trends from 2012 to 2020 in fossil and livestock emissions.

1. Introduction

All GOSAT-derived emissions and corresponding inputs/algorithms are available at [https://doi.org/10.5281/zenodo.15786798].
Jupyter / python code at [https://zenodo.org/records/16921536] shows how to compare these GOSAT derived emissions to inventories.

Methane is a potent greenhouse gas that plays a significant role in atmospheric warming (Saunois et al., 2020). Methane is emitted from multiple anthropogenic sources including livestock, oil and gas exploitation, manure, rice cultivation, wastewater, solid waste, and coal mining, and from natural sources, particularly wetlands. Methane is also the main component of natural gas, a valuable global commodity that can pose safety risks when it leaks. Accurate and verifiable estimates of its emissions are essential for tracking progress and guiding effective mitigation strategies, and for accounting for the economic value of energy waste (IEA, 2025; World Bank, 2025). Gridded methane emission inventories, such as the gridded United States Environmental Protection Agency's Greenhouse Gas Inventory (EPA GHGI), the Emissions Database for Global Atmospheric Research 2024 release (EDGAR 2024), and the National Oceanic and Atmospheric Administration's Fuel-based Oil and Gas inventory (NOAA FOG), are widely used for comparing sectoral emissions, primarily at the regional scale, to atmospheric data (EPA, 2023; Maasakkers et al., 2023; Crippa *et al*., 2020, 2024; Francoeur et al., 2021; Kruskamp *et al*., 2025). However, discrepancies in how the inventories are generated, e.g. from

emission factor assumptions, activity data, and/or spatial proxies and resolution can result in substantial variation in both the magnitude and sectoral attribution of emissions (Hristov et al., 2017; Alvarez et al., 2018; Maasakkers et al., 2021; Petrescu et al., 2024; Gordon 2025). In some cases, differences between inventories can be as large as the emissions themselves (Figure 1), complicating the evaluation of national and regional emission trends. Verification of their underlying parameterizations is often limited by spatiotemporal mismatches between empirical measurements and inventory assumptions. Moreover, differences between activity-based emissions and flux estimates based on observations combined with atmospheric modeling (e.g., top-down atmospheric inversions) can far exceed the changes inferred from the observed growth in atmospheric methane concentrations (Nisbet et al., 2019; Worden et al., 2022). As a result, tracking mitigation progress using bottom-up inventories alone could be unreliable without independent observational constraints. In addition to these uncertainties, emissions missing in the inventories pose another significant challenge. For instance, sporadic high emitters in both fossil fuel production and waste management, often caused by mechanical failures, may not be captured in traditional inventories (Cusworth et al., 2020, 2024; Sherwin et al., 2024); consequently, the magnitude of these emissions remains poorly understood.

To evaluate potential uncertainties in bottom-up inventories, top-down emissions estimates derived from satellite observations, such as those from the Greenhouse Gases Observing Satellite (GOSAT), provide a valuable, independent constraint. These atmospheric measurements inherently capture all emissions influencing methane concentrations, including unreported or underestimated sources, and therefore offer a more comprehensive view of total methane emissions. However, the resulting estimates and their information content (spatial resolution + uncertainties) depend strongly on the observational sampling, sensitivity of the observation to the emissions, choice of a priori fluxes, and the inversion regularization. Consequently, over regions with limited sampling, e.g., due to clouds or low sunlight, top-down analyses have greatly reduced sensitivity to nearby emissions, so the estimates there simply reflect the *a priori*. In contrast, emissions inferred for regions with ample sampling are more likely to accurately represent local sources. The focus of this paper is to demonstrate how this GOSAT-based benchmark can be used to evaluate alternative gridded inventories while accounting for its variable information content as discussed next.

Method and Data

Accounting for choice of *a priori* and inversion regularization: Comparisons between satellite-based top-down fluxes and activity-based inventories must account for the variation in sensitivity of the data to emissions and choice of *a priori*, otherwise substantial uncertainty (also known as *smoothing error*) is introduced into the comparison (Rodgers, 2000; Worden et al., 2022, 2023). Smoothing error in this context can be mitigated for these comparisons by at least three ways: 1) by using the inventory as the *a priori* in the inversion or 2) by applying an inversion operator to the inventory being compared (the inversion operator depends on the inversion *a priori* and what is called the averaging kernel matrix, Appendix B) or 3) by adjusting the GOSAT based estimate using the gridded inventory and the averaging kernel matrix to replace the effect of the original prior (also known as prior swapping).

In the first scenario, recalculating the inversion and subsequently comparing to the *a priori* is computationally expensive (e.g., Nesser et al., 2024 and references therein) as it involves minimizing a cost function of gridded emissions vector (e.g. **z)** that typically has the following form:

$$\mathbf{C} = ||\mathbf{y} - \mathbf{F}(\mathbf{z_A})||^2_{\mathbf{S_n^{-1}}} + ||\mathbf{z} - \mathbf{z_A}||^2_{\mathbf{S_A^{-1}}} \quad (1)$$

Where **y** is a state vector representing concentrations (e.g. total column methane or XCH_4), the forward model $\mathbf{F(z_A)}$ in this case is the Goddard Earth Observing System – Chemistry model (GEOS-Chem) driven by a distribution of *a priori* emissions ($\mathbf{z_A}$). The matrix $\mathbf{S_n}$ represents the measurement error covariance for the total column data and the matrix $\mathbf{S_A}$ represents the uncertainty (or covariance) in our *a priori* emissions. For the benchmark described in this paper, the vector **z** represents the spatial distribution of anthropogenic emissions by sector, in this case livestock, waste, coal, rice, oil&gas. Wetlands and fire emissions are also estimated with the GOSAT data and the effect of jointly estimating these emissions are included in the posterior covariance and uncertainties of the anthropogenic emissions estimate (Worden *et al.,* 2022, 2023*)*.

The estimate for the converged solution, $\hat{\mathbf{z}}$, can be related to the "true distribution" of the emissions ($\mathbf{z}$) with the following (e.g. Rodgers 2000).

$$\hat{\mathbf{z}} = \mathbf{z}_A + \mathbf{A}(\mathbf{z} - \mathbf{z}_A) \quad (2)$$

where for clarity we have not included the uncertainty terms (see Appendix B). The averaging kernel matrix $\mathbf{A}$ is a function of the *a priori* and posterior covariance, $\hat{\mathbf{Z}}$ and $\mathbf{Z}_A$ (see Appendix B for a description of uncertainties and prior covariances) and describes the sensitivity of the distribution of estimated emissions to the true state ($\mathbf{A} = \frac{\partial \hat{\mathbf{z}}}{\partial \mathbf{z}}$). Approach #2, which is to apply an inversion operator to the inventory, is equivalent to replacing $\mathbf{z}$, or the "true distribution" of emissions, with the alternative inventory, $\mathbf{z_I}$ in Equation 1; this approach is commonly used for data assimilation or for comparing atmospheric trace gas profiles from models or in situ measurements to remotely sensed measurements (e.g. Wecht *et al*. 2014, Herman *et al*. 2014). This revised estimate can be compared to $\hat{\mathbf{z}}$ while accounting for the *a priori* and regularization choices made in the inversion described by Equation 1. Approach #3 (or prior swapping) instead involves replacing $\mathbf{z_A}$ with the alternative inventory (e.g. Rodgers and Connor 2003)

$$\hat{\mathbf{z}}_{new} = \hat{\mathbf{z}} - (\mathbf{I} - \mathbf{A})\mathbf{z}_A + (\mathbf{I} - \mathbf{A})\mathbf{z_I} \quad (3)$$

And is equivalent to re-running the inversion described by Equation (1) with this alternative *a priori*.

As approaches 2 and 3 are linear operations, they result in equivalent comparative differences as shown in Appendix B. In this manuscript we use the inversion operator approach (Equation 2) for consistency with previous publications (e.g. Worden et al., 2022, 2023).

Sector Based Attribution: We use estimates of gridded integrated fluxes from a GEOS-Chem based inversion using GOSAT XCH_4 data as described in Qu *et al.* (2022,2024). We use a Bayesian-based sectoral partitioning approach (Appendix A, Worden et al., 2022, 2023) to project these top-down integrated fluxes to emissions by sector at a 1° × 1° resolution. This approach characterizes the inversion solution by providing a posterior covariance for the solution and provides the "inversion operator" (Equation 2) that, when applied to a gridded inventory,

enables the comparison to inversion results by capturing the influence of the inversion's prior emissions and the sensitivity of the satellite observations to those emissions (Rodgers, 2000).

Inventories: (See Appendix C for more detail) The inventories we compare include EDGAR 2024 (Crippa et al. 2024), the gridded U.S. EPA GHG inventory (GHGI) (Maasakkers et al. 2023), and NOAA FOG (Francoeur et al. 2021). The EDGAR and GHGI inventories provide information about methane emissions across multiple sectors (e.g., livestock, waste, oil and gas, coal, rice). The approaches estimating these emissions vary, with EDGAR down-scaling national totals to finer scales using spatial information about the sources using global datasets while the GHGI gridded inventory reflects emission factors and activity data used in the EPA U.S. Greenhouse Gas Inventory. In contrast, NOAA FOG focuses specifically on fossil methane emissions and is a hybrid inventory that integrates atmospheric CH_4 and NO_2 observations with activity-based NO_2 metrics (Francoeur et al. 2021). While these inventories show considerable overlap in the location of emissions, differences can be large, even when aggregating from the original 0.1 degree grid of the inventories to the 1 degree grid shown for Figure 1.

As stated previously, our goal for this study is to demonstrate a benchmark for U.S. methane emission gridded inventories and their changes from 2012 to 2020. These comparisons are documented and publicly accessible at Zenodo (see data availability); Jupyter notebooks are provided here that demonstrate how to compare gridded inventories to GOSAT-based emissions. These benchmarks will be updated as newer datasets, such as inverse analyses using Sentinel-5P TROPOMI (Tropospheric Ozone Monitoring Instrument) observations, become available (e.g., Nesser et al. 2024; Hancock et al. 2025). Readers unfamiliar with the Bayesian attribution framework, the GOSAT inversion, or the specific inventories compared are encouraged to consult the appendices, where these methods are summarized, or our previously published work on the subject (Cusworth et al. 2021; Worden et al., 2022,2023).

2. Integrated total and sectoral USA emissions for 2015

Table 1 summarizes U.S. methane emissions by sector for 2015, based on the GOSAT data and the sectoral attribution approach described in this study (Appendix A). The error characterization (Appendix B) includes uncertainties from the *a priori* as well as measurement and model systematic error. The prior emissions are taken from Worden *et al*. (2023). Table 1 also shows a quantity called the Degrees of Freedom for Signal (DOFS), which is given by the trace of the averaging-kernel matrix for the corresponding state-vector elements in **z.** The DOFS describe the extent to which the estimate is informed by observations rather than prior assumptions (Appendix B), as well as the spatial information content. For example, from Equation 2, if $\mathbf{A} \approx \mathbf{0}$ (equivalent to DOFS = 0), observations say essentially nothing about the emissions and the estimate reduces to the prior. If **A** is the identity matrix, then the DOFS equals the number of state-vector elements and the estimate exactly reflects the true distribution, modified by the expected uncertainties (Appendix B). The DOFS reported in Table 1 refer to the spatially distributed estimate, not for the total emissions value. Hence, DOFS > 1 means there is at least some spatial information for that sector's estimate.

For this GOSAT-based benchmark, the highest information content is available for total, livestock, and oil and gas (O&G) emissions, while waste emissions estimates are only moderately constrained by the data, and rice and coal emissions have limited observational information. This variability in information content underscores the need for careful interpretation of top-down estimates, particularly when examining spatial and sectoral patterns or trends.

Table 1: GOSAT-Based CONUS Anthropogenic Emissions and Information Content by Sector (2015

Sector	**Emissions (Tg CH_4/yr)**	***A priori* (Tg CH_4/yr)**	**DOFS***
Total	29.4 ± 1.5	28.2±2.0	3.4
Livestock	10.3 ± 1.2	9.2 ± 1.4	1.8
Rice	0.4 ± 0.1	0.4±0.1	0.0
Waste	4.5 ± 0.6	5.6±0.8	0.6
Oil & Gas	11.1 ± 0.9	9.9±1.2	1.0

Coal	3.1 ± 0.3	3.1±0.3	0.1	

Table 2 compares our emissions to previous inversions using atmospheric data and to the inventories discussed in this paper (Appendix C). As can be seen in Table 2, our atmospheric-based emissions are generally consistent with other studies, typically within 1–2 standard deviations of the reported uncertainties, even though each study uses different priors, has different systematic errors, and has different sensitivity to the underlying emissions. These comparisons also show that total emissions from atmospheric-based inversions are typically larger than activity-based estimates, with the livestock and oil and gas sectors responsible for most of the discrepancy.

Table 2: Comparison of Methane Emissions by Study. All totals are CONUS anthropogenic; years as listed;

(All values in Tg CH_4/yr)

Study	Total	Livestock	Rice	Waste	Oil & Gas	Coal
(Atmospheric Inversions)						
GOSAT (2015 This Work)	29.4 ±1.5	10.4±1.2	0.4 ±0.1	4.6±0.6	11.1 ± 0.9	3.1 ±0.3
GOSAT (2019)[1]	27.3 ± 3	9.9 ± 0.9	0.3±0.1	4.0±0.7	10.3 ± 1.0	2.8 ±0.4
TROPOMI (2019)[2]	30.9 ± 0.9	10.4 ± 0.3	N/A	6.9±0.6	10.4 ± 0.3	1.5 ±0.4
GOSAT + Surface (2009–2020)[3]	29.1±0.5	8.8 ± 0.3	N/A	4.2±0.1	14.1 ± 0.2	2 ± 0.4
GOSAT (2010–2015)[4]	31 ± 1.0	9.4 ± 0.4	0.4±0.2	6.2±0.2	11.1 ± 0.6	3.2±0.1
In Situ (2007-2008)[5]	33.4 ± 2	N/A	N/A	N/A	N/A	N/A
In Situ (2003)[6]	32.4 ± 5	N/A	N/A	N/A	N/A	N/A
(Activity Models and Year)						
GHGI (2015)[7]	23.7±2.1	8.9±1.4	0.6±0.3	4.8±1.4	6.9±1	2.5±0.4
EDGAR (2015)[8]	25.7±2.1	8.6±1.4	0.3±0.1	4.3±1.3	10.1±1	2.4±0.4

NOAA FOG (2015)[9]	14.1 ± 2

Table 2: Comparison of Methane Emissions by Study. All totals are CONUS anthropogenic emissions for the years listed. Values are reported in Tg CH_4 yr^{-1}. Atmospheric inversions exclude natural sources and fire emissions where sectoral separation is available. Activity-based estimates include the gridded EPA GHGI, EDGAR 2024, and NOAA FOG inventories evaluated in this study. References: (1) Worden et al. (2022), (2) Nesser et al. (2024), (3) Janardanan et al. (2024), (4) Maasakkers et al. (2019), (5) Miller et al. (2013), (6) Kort et al. (2008), (7) Maasakkers et al. (2016, 2023), (8) Crippa et al. (2024), and (9) Francoeur et al. (2021).

2.1 Oil and Gas Emissions (GOSAT, FOG, EPA, and EDGAR)

We next compare the GOSAT-based emissions for O&G to those from NOAA FOG, GHGI, and EDGAR inventories. In particular, we demonstrate how applying the inversion operator to these inventories modifies our interpretation of the comparison.

Spatial Distribution for 2015: Figures 2 through 4 compare the spatial distribution of U.S. oil and gas (O&G) methane emissions in 2015 from the GOSAT inversion with those from the FOG, GHGI, and EDGAR (2024 release, Crippa et al., 2024) inventories respectively. These comparisons demonstrate the importance of accounting for the varying information content of the GOSAT inversion, which is influenced by both the prior emissions used in the inversion and the sensitivity of the aggregated satellite observations to underlying emission patterns (Worden et al., 2023 and references therein). In Figure 2, the upper left panel (a) shows the GOSAT based estimate. The upper right panel (b) shows the original FOG emissions. The middle left panel (c) shows the difference between the top two. The middle right panel shows the difference between FOG emissions and GOSAT based emissions after applying the inversion operator (denoted AK). All figures use 1x1 degree gridding. The bottom right panel (E) shows the diagonal of the averaging kernel (or DOFS) corresponding to that location for oil and gas emissions. As seen in the left panel of Figure 2, significant regional discrepancies between the GOSAT and FOG inventories exist, with similar magnitude differences as shown in Figure 1. However, after

applying the inversion operator (Equation 2) to the FOG inventory (labeled FOG AK), many of these differences are greatly reduced (middle right panel)

Small differences between GOSAT and the inventory, after applying the inversion operator, can also occur because of limited sensitivity, as indicated by the DOFS, for example over the Bakken region of North Dakota. As discussed previously and shown in Equation 2 and Appendix B, in such cases the difference between the GOSAT estimate and the inventory adjusted by the inversion operator should be close to zero, because both terms reduce to $\sim z_A$. In contrast, the GOSAT estimate shows increased sensitivity to emissions in Oklahoma, Texas, and Louisiana. Based on this comparison, and on the integrated total emissions in the next section, we conclude that the GOSAT estimate does not falsify the spatial distribution of methane emissions posited by the FOG oil and gas inventory.

Interpreting Comparisons between GOSAT, EDGAR, and GHGI emissions:

Comparisons between GOSAT and EDGAR (Figure 3) and between GOSAT and EPA GHGI (Figure 4) show larger discrepancies, even after applying the inversion operator, particularly in northwest Colorado, Texas, Oklahoma, and Louisiana. These patterns indicate substantial inventory uncertainties in well-observed regions with intensive oil and gas activity. Some regions are sparsely observed by GOSAT, so their contributions may be important but their uncertainties cannot be reliably assessed with this benchmark. When measurement cost is a constraint, the discrepancy hotspots identified here are high-value targets for additional observations, with expanded coverage of under-sampled regions as resources allow.

Previous studies (e.g., Alvarez et al. 2018; Cusworth et al. 2022; Sherwin et al., 2024) have shown that a small number of high emitters (e.g., <2%; Sherwin et al., 2024), likely due to unplanned mechanical failures, contribute disproportionately to the fossil methane budget. These sources are likely underrepresented or missing from activity-based inventories. The agreement between FOG and GOSAT supports this conclusion, as the FOG inventory integrates atmospheric CH_4 with NO_x observations and activity metrics; these regional CH_4 observations capture emissions under-represented in purely bottom-up approaches. If such super-emitters are

entirely responsible for the discrepancies between GOSAT and the EPA GHGI and EDGAR inventories, then comparisons between the GOSAT, EPA, EDGAR, and FOG O&G emissions in Table 2 suggest these sources are undercounted by ~7 Tg CH_4/yr of reported natural gas emissions, far exceeding previous estimates, as previously documented in other studies (e.g., Alvarez et al. 2018; Cusworth et al. 2022; Sherwin et al., 2024; Zavala-Araiza et al. 2015).

Integrated totals for 2015: Figure 5 compares integrated total oil and gas (O&G) emissions derived from GOSAT with those from the FOG, GHGI, and EDGAR inventories.

Before applying the inversion operator, total FOG emissions are estimated at 14.1 ± 2 Tg CH_4 yr^{-1}. We assumed the same prior covariance structure ($\mathbf{Z_A}$, Appendix B; Worden et al., 2022, 2023) for FOG as for the GOSAT *a priori*. This yields a smaller total uncertainty (2 Tg CH_4 yr^{-1}) than the ~2.8 Tg CH_4 yr^{-1} uncertainty for total FOG O&G emissions inferred from a Monte Carlo analysis of NO_x activity data (Francoeur *et al*., 2021). Using a different covariance structure that is consistent with the stated uncertainty in total emissions could therefore change conclusions about whether the GOSAT estimate falsifies the FOG inventory, and the inversion-operator methodology in Equation 2 would allow this. However, a full covariance is required, with explicitly computed off-diagonal terms such that, when projected to a single number, it reproduces the expected uncertainty reported in, for example, Francoeur et al. (2021).

After applying the inversion operator, the FOG total is reduced to 11.4 Tg CH_4 yr^{-1}. The uncertainty shown for the modified FOG estimate (denoted FOG-AK) reflects the uncertainty in the difference between the GOSAT-based estimate and the FOG-AK estimate (Appendix B Equation 15), not the uncertainty of the FOG-AK estimate itself. Because the FOG-AK estimate is consistent with the GOSAT-based inversion within the reported uncertainty, this comparison suggests that the GOSAT estimate does not falsify the original, higher FOG total of 14.1 Tg CH_4 yr^{-1}.

Figure 5 also shows comparisons to GHGI and EDGAR. For these inventories, uncertainties prior to applying the inversion operator are derived using the same prior covariance structure as for the GOSAT a priori, because published full covariances are not readily available.

In contrast to the FOG comparison, both the EPA and EDGAR estimates, with or without application of the inversion operator, are inconsistent with the GOSAT-based inversion. Their differences lie well outside the post-operator uncertainty shown for each inventory. As shown in Figures 3 and 4 these differences are spatially located primarily in the Texas, Oklahoma, and Louisiana regions. As noted previously, additional measurements here are therefore likely to reduce uncertainties in the USA O&G methane budget.

Integrated Totals: 2012–2020: Figure 6 shows annual methane emissions from 2012 to 2020. Despite substantial increases in oil and gas production over this period, all gridded inventories and the GOSAT top-down estimates show no significant change in total U.S. methane emissions, although the FOG inventory may have a slight increase. This apparent disconnect between rising production and stable emissions has been noted in several studies and is commonly attributed to improvements in production efficiency, leak detection, and emissions control technologies (e.g., Lu et al., 2023). EPA GHGI supports this conclusion, showing relatively flat changes in fossil fuel methane emissions over the same period. This stability in the activity estimate is explained by offsetting trends, including a decline in exploration emissions due to fewer well completions, the adoption of lower-emitting equipment, and stable or slightly declining well counts (Maasakkers et al. 2023). For instance, while natural gas production increased by 26% and crude oil production by 67%, the number of active gas and oil wells remained roughly constant, declining slightly over the period. Emissions from gas systems were flat overall, with increases in gathering and boosting offset by decreases in production and processing. Similarly, petroleum system emissions rose by just 11% due to a significant drop in exploration-related emissions (Maasakkers et al. 2023).

2.2 Livestock Emissions (GHGI and EDGAR)

Spatial Distribution for 2015: Similar to Figures 2-4, Figures 7 and 8 show the spatial distribution of livestock methane emissions from GOSAT, EDGAR, and GHGI data. The FOG inventory is limited to oil and gas emissions and is therefore excluded from this and subsequent comparisons. Methane emissions from livestock generally scale with herd size, particularly dairy and beef cattle. Dairy cows typically emit more than twice as much methane as beef cows, due to higher enteric fermentation (Wolf et al., 2017; Hristov et al., 2017). Emissions vary geographically with management and environmental conditions (for example grazing practices, feed quality, and temperature, Wolf et al., 2017). Inventories account for this using region-specific emission factors, but if the factors used are not representative of actual local conditions, the resulting difference between the atmospheric based and activity based emissions should be spatially structured rather than random. Consistent with this, we observe systematic regional biases relative to the GOSAT-based estimates: inventories in California and the northern states are higher than GOSAT, whereas inventories in northern Texas are lower.

Integrated Total for 2015: Figure 9 compares integrated livestock methane emissions from GOSAT with GHGI and EDGAR inventories, each shown with and without the inversion operator applied. The GHGI and EDGAR totals differ modestly. The EPA total lies slightly outside the GOSAT uncertainty range, while the EDGAR total falls within it. However, agreement in totals does not imply agreement in spatial patterns. For EDGAR in particular, closer total agreement with GOSAT coincides with offsetting regional deviations, with positive differences in parts of the Midwest and negative differences in California. These cancellations reduce the apparent mismatch in the national total, which underscores the importance of evaluating spatial variability alongside integrated totals. Overall, comparisons of integrated totals and spatial patterns indicate substantial remaining uncertainty in livestock emissions. Additional measurements over California and the Midwest, especially in the Texas and Oklahoma region, would likely reduce this uncertainty.

Integrated Totals for 2012-2020: Figure 10 (and Table 2) shows comparisons between the integrated total livestock emissions from the GOSAT based inversion and the GHGI and EDGAR inventories. The GOSAT-based estimate as well as those from the GHGI and EDGAR

inventories do not observably change within the calculated uncertainties, except possibly for the year 2019. We therefore conclude that GOSAT based livestock emissions cannot falsify the posited (flat) trends from activity data (Maasakkers et al. 2021).

2.3 Waste (GHGI and EDGAR)

Figures 11 and 12 show the spatial distribution of methane emissions from the waste sector based on GOSAT, GHGI, and EDGAR estimates and Figure 13 shows the integrated total for 2015. The largest differences are for California for the EDGAR / GOSAT comparison. The integrated waste sector methane emissions from GOSAT are estimated at 4.5 ± 0.6 Tg CH_4/yr, while both GHGI and EDGAR report lower values of 4.2 ± 0.3 Tg CH_4/yr. These differences are not statistically significant, as the GOSAT estimate lies within the uncertainty range of both inventories (after applying the inversion operator). However, there is very limited spatial information content in the GOSAT waste estimate (~0.6 DOFS total). Consequently, the spatial differences shown in the right-bottom panel don't show meaningful differences between the inventories and the GOSAT waste estimate for most of the country. Because of this limited sensitivity we do not compare temporal changes in the waste emissions.

3. Summary and Future Directions

Top-down methane emissions estimates vary in their information content depending on the emission sector and observing system. For these GOSAT based emissions estimates, information content is greatest for oil and gas and livestock, so these sectors are best suited for inventory evaluation using the results shown here. Waste, coal, and rice exhibit lower information content in this analysis because GOSAT does not adequately sample methane variability attributable to those sources. Even so, our information-content-based comparison identifies where additional measurements would yield the largest uncertainty reductions in gridded inventories.

In particular, our results highlight the need for targeted measurement campaigns, especially in the Texas, Oklahoma, and Louisiana drilling basins, where additional data can most effectively reduce inventory uncertainties. For the livestock sector, California and Northern

Texas stands out as key regions where improved activity based and atmospheric methane observation can have the highest impact. These findings underscore the importance of prioritizing high-emitting or uncertain regions to refine national methane budgets.

Beyond regional targeting, improving inversion resolution is also key. Higher-resolution flux estimates, whether through satellites like TROPOMI or plume-resolving instruments (e.g., Jacob et al. 2022; Pandey et al. 2025 and refs therein), are particularly needed for sectors such as waste, coal, and oil and gas, where coarse-resolution inversions struggle to isolate source signals. In particular, integrating plume-resolving and area-flux estimates enhances the sectoral attribution of emissions and improves the information content for inventory evaluation (Pandey *et al*. 2025).

(**Trends**) Inversions conducted using GOSAT data and GEOS-Chem (see references in Table 2), show no discernible trend over the analysis period, which is consistent with all three gridded inventories discussed in this manuscript. However, the fact that other inversions show different trends highlights the importance of benchmarking approaches (Janardanan et al. 2024), not only for validating inventories but also for identifying uncertainties in inversion outputs themselves. These differences matter for informing effective remediation strategies and setting realistic expectations for emission reductions.

As satellite constellations improve in spatial resolution, sampling, and accuracy, top-down flux estimates become more accurate at higher spatial resolution (e.g., Jacob et al., 2022). Using TROPOMI, Nesser et al. (2024) produced a 2019 North American emissions map with a degree of freedom for signal (DOFS) of ~772, more than two orders of magnitude higher than in our GOSAT record, driven by a similar increase in observations. This resolution enables explicit estimation of many large sources, including landfills. East et al. (2025) extended this approach to global coverage at similar ~25 km gridding. Building a benchmark from the combined record will help evaluate how countries have managed emissions before and after the Global Methane Pledge, which targets a 30 percent reduction from 2020 to 2030. Our approach shows how inventories can be benchmarked against these improved flux estimates to reduce uncertainty, especially smoothing error, without re-running inversions with inventory priors. Combining high-resolution, independent datasets will support more accurate methane inventories, clarify source trends, and inform effective mitigation strategies.

Appendices

Appendix A: GOSAT Methane Fluxes and Projection to USA Emissions by Sector

(**Overview**) Yearly sectoral emissions by region based on the satellite data are generated in a two step process. The first step is to quantify global integrated fluxes using total atmospheric column methane data from the Japanese GOSAT (Greenhouse gases Observing SATtellite) instrument (Parker *et al*. 2011) and the GEOS-Chem model (Zhang *et al*., 2021). The approach used to generate fluxes has been extensively documented in past literature (e.g. Zhang et al., 2021, Qu et al., 2024), and we refer the reader to these articles. The state vector for this inversion include 1) yearly anthropogenic methane emissions between 2010 and 2022 at a gridding of 5x4 degrees (longitude/latitude) and we use the estimates between 2012 and 2020 for this study, 2) wetland methane emissions for specified regions for each month between 2010 to 2022), and 3) the yearly hemispheric methane sink. The second step (next section) is a linear estimate based on an optimal estimation sectoral emissions attribution approach (Cusworth *et al*. 2021; Worden *et al*. 2022) that projects the integrated anthropogenic fluxes to emissions by sector and trends at the same 5x4 degree gridding and then again at 1x1 degree (lon/lat) gridding over the USA. This projection accounts for the prior distribution and uncertainties in the emissions (e.g. Worden et al. 2022). We next provide more detail on projection/attribution methodology as it is relevant to the benchmarking methodology that is the focus of this paper.

(**Sectoral attribution of fluxes to emissions**) We use a Bayesian based approach to project the fluxes described in the previous section (at 5x4 degrees lon/lat) to emissions by sector at 1x1 degree. The full methodology is described in Cusworth et al. (2021) and first applied to methane fluxes in Worden et al. (2022) and again in Worden et al. (2023). This approach is equivalent to swapping the *a priori* assumptions, given by $\mathbf{x_A}$ and $\mathbf{S_A}$, to a different state vector $\mathbf{z_A}$ (and *a priori* covariance $\mathbf{Z_A}$) when a linear relationship between the different state vectors **x** and **z** exist. The approach provides the full posterior and prior covariances and priors needed to account for the varying information content of satellite based emissions estimates when comparing these emissions to either each other (e.g. between years) or to inventories (Worden et al. 2023) or to other estimates. We refer the reader to these papers, starting with Cusworth et al. (2021) for the primary derivation, and summarize here.

Given a linear mapping between one state vector and another (e.g. between fluxes **x** at 5x4 degrees versus emissions **z** at 5x4 degrees or alternatively emissions at 1x1 degree):

$$\mathbf{x} = \mathbf{M}\mathbf{z}, \tag{4}$$

As discussed in Worden et al. (2023), the solution for projecting fluxes back to emissions takes the form:

$$\hat{\mathbf{z}} = \mathbf{z}_A + \hat{\mathbf{Z}}\mathbf{M}^T\hat{\mathbf{S}}^{-1}\left[\left(\mathbf{I} - \hat{\mathbf{S}}\mathbf{S}_A^{-1}\right)(\mathbf{x}_A - \mathbf{M}\mathbf{z}_A) + (\hat{\mathbf{x}} - \mathbf{x}_A)\right] \tag{5}$$

where the $\hat{\mathbf{z}}$ and $\mathbf{z}_A$ is the posterior and prior emissions state vector respectively with posterior and prior error covariance $\hat{\mathbf{Z}}$, $\mathbf{Z}_A$ respectively.

The posterior emission error covariance matrix $\hat{\mathbf{Z}}$ is calculated explicitly given $\mathbf{M}$, $\mathbf{S}_A$, $\hat{\mathbf{S}}$, and prior emissions error covariance matrix $\mathbf{Z}_A$:

$$\hat{\mathbf{Z}} = \left(\mathbf{M}^T\left(\hat{\mathbf{S}}^{-1} - \mathbf{S}_A^{-1}\right)\mathbf{M} + \mathbf{Z}_A^{-1}\right)^{-1} \tag{6}$$

Here, the $\hat{\mathbf{S}}$ is the posterior covariance for the fluxes described in the Qu *et al*. (2024), with prior error covariance $\mathbf{S}_A$, given as a diagonal matrix with values of 0.5 (squared). The $\mathbf{I}$ is the identity matrix. The prior covariances for each emission category (livestock, waste, rice, coal, oil and gas, and fires) are described in Worden et al. (2022) and Worden et al. (2023).

Uncertainty Calculation

After projecting the estimate for integrated fluxes at 5x4 degrees ($\hat{\mathbf{x}}$) to emissions by sector at 1x1 degree ($\hat{\mathbf{z}}$), we can describe $\hat{\mathbf{z}}$ using Equation 2 with corresponding averaging kernel as discussed in the introduction (and now including uncertainties):

$$\hat{\mathbf{z}} = \mathbf{z}_A + \mathbf{A}(\mathbf{z} - \mathbf{z}_A) + \boldsymbol{\delta}_n + \boldsymbol{\delta}_m \quad (7)$$

where $\boldsymbol{\delta}_n$ and $\boldsymbol{\delta}_m$ are the errors from measurement error and model error respectively. The measurement and model errors are discussed in Worden *et al.* (2022, 2023). The error covariance for $\hat{\mathbf{z}}$ is then given by:

$$E||\hat{\mathbf{z}} - \mathbf{z}\ || = \mathbf{Z_{total}} = (\mathbf{I} - \mathbf{A})\mathbf{Z_A}(\mathbf{I} - \mathbf{A})^{\mathbf{T}} + \mathbf{S_n} + \mathbf{S_m} \quad (8)$$

Note that the inverse of the Hessian (Equation 6) is equivalent to the first two terms (Worden *et al*. 2004; Bowman *et al*. 2006):

$$\hat{\mathbf{Z}} = (\mathbf{I} - \mathbf{A})\mathbf{Z_A}(\mathbf{I} - \mathbf{A})^{\mathbf{T}} + \mathbf{S_n} \quad (9)$$

Equation 9 allows us to separate the "smoothing error" (the first term on the RHS of Equation 9), from the measurement error in order to better evaluate comparisons between the GOSAT and inventory methane estimates as discussed in the next section.

In order to calculate the emissions for either a region (e.g. USA) or a category of emissions (e.g. rice), we must first sum the corresponding elements of the state vector:

$$\mathbf{z_i} = \mathbf{h_i}\hat{\mathbf{z}}, \quad (10)$$

Where $\mathbf{h_i}$ is a column vector that projects the desired elements of $\hat{\mathbf{z}}$ to region or sector i, $\mathbf{z_i}$. As discussed in Worden et al. (2022), the uncertainty of $\mathbf{z_i}$ is then given by

$$\sigma_i^2 = \mathbf{h_i}\mathbf{Z_{total}}\mathbf{h_i^T} \quad (11)$$

As discussed in these previous papers, this uncertainty calculation accounts for the effects of cross-terms (e.g. wetlands, OH, fires). Equation (11) is what is used to calculate the uncertainties shown in the figures and the tables in this paper.

Appendix B: Bayesian / Optimal Estimation Approach for Comparing Inventory to top-down Inversion

To compare a 0.1° × 0.1° inventory with top-down fluxes based on an inversion of atmospheric data, we first project the inventory to the same spatial scale as the top-down fluxes and then account for the sensitivity of the top-down estimates. The native resolution of the gridded inventories is 0.1°, provided by sector. In contrast, the GOSAT based fluxes are at a coarser resolution of 5° × 4° (longitude × latitude) and represent integrated fluxes (Qu et al., 2024) with no sectoral specificity in each grid. Our approach is to first re-grid the inventory to 1° × 1°, while retaining sectoral distinctions (e.g., livestock, waste, rice, coal, oil & gas). As discussed in the following paragraph, we then project the 5° × 4° GOSAT-inverted methane fluxes to sector-specific emissions at 1° × 1° resolution as discussed in Appendix A. We selected this intermediate resolution to better represent national emission patterns, as a 5° × 4° grid can cause significant overlapping flux contributions from neighboring countries such as the United States, Canada, and Mexico.

The comparison approach is described in Worden *et al*. (2023) and summarized here. We next project the inventory ($\mathbf{z_i}$) through the "inversion operator" (Equation 2) in order to account for the choice of a priori in the inversion and the sensitivity of the emissions (Rodgers 2000, Worden et al., 2022, 2023).

$$\hat{\mathbf{z}}_i = \mathbf{z}_\mathrm{A} + \mathbf{A}(\mathbf{z}_i - \mathbf{z}_A) \quad (12)$$

Where $\mathbf{z_A}$ is a vector describing the *a priori* methane emissions used for the top-down estimate and **A** is the averaging kernel matrix calculated for that inversion. The averaging kernel matrix is a function of the prior and posterior covariance, $\hat{\mathbf{Z}}$and $\mathbf{Z_A}$:

$$\mathbf{A} = \mathbf{I} - \hat{\mathbf{Z}}\mathbf{Z_A}^{-1} \quad (13)$$

The DOFS shown in Table 1 are calculated by taking the sum of diagonal elements (or trace) of the averaging kernel corresponding to the sector.

After application of the inversion operator a comparison of these modified inventory emissions with the GOSAT- based emissions (Cusworth et al. 2021, Worden et al. 2023, Appendix A) is given by:

$$\hat{\mathbf{z}} - \hat{\mathbf{z}}_i = \mathbf{A}(\boldsymbol{\delta_i}) + \boldsymbol{\delta_n} + \boldsymbol{\delta_m} \quad (14)$$

Where $\boldsymbol{\delta_i}$ is the uncertainty in the inventory, $\boldsymbol{\delta_n}$ is the uncertainty in the inversely estimated emissions due to noise in the atmospheric data, and $\boldsymbol{\delta_m}$ is the uncertainty in the model used to project concentrations to emissions. The effect of the prior, $\mathbf{z_A}$, is also removed in this comparison described by Equation 14 so that the inventory can be compared to the satellite based emissions without this large effect of smoothing error on the comparison (see subsequent figures and supplemental). The error of the difference between satellite estimate and this adjusted inventory is then the expectation of the difference:

$$E||\hat{\mathbf{z}} - \hat{\mathbf{z}}_i|| = \mathbf{A}\mathbf{S_i}\mathbf{A}^{\mathbf{T}} + \mathbf{S_n} + \mathbf{S_m} \quad (15)$$

Where $\mathbf{S_i}$ is the covariance for the inventory uncertainties $\boldsymbol{\delta_i}$, $\mathbf{S_n}$ is the measurement error projected to emissions, and $\mathbf{S_m}$ is the model error. Note that $\mathbf{S_n}$ is directly calculated from the inversion (Worden et al. 2023). The final term in Equation 15, the model error, can be highly challenging to quantify. Previous studies have pointed towards the vertical mixing in models as being the largest source of model error; too much or too little methane (or other trace gas) at the

surface as a result of incorrect mixing leads to inaccurate surface flux calculations (e.g. Jiang et al. 2013; Schuh et al. 2019; Mcnorton et al. 2020). These studies show that this effect is largest in the tropics where there is significant convection with an uncertainty that is about the same size as the data uncertainty. On the other hand, the mid-latitudes likely have smaller uncertainties of this type because of smaller uncertainties related to vertical mixing. For the purpose of this study we assume the model error is the same magnitude as the observation error $\mathbf{S_n}$; however continued advances are needed in both quantifying and mitigating this term, and how it affects the emissions estimates, in order to improve confidence in the comparisons between inventories and satellite data.

Note that if the GOSAT-based emissions are directly compared to the inventory without first passing the inventory through the inversion operator, then the uncertainties in the comparison are much larger and less meaningful as they include both the smoothing error of the data and the full uncertainty of the inventory:

$$E||\hat{\mathbf{z}} - \mathbf{z}_i|| = \mathbf{S_i} + \mathbf{S_n} + \mathbf{S_m} + \mathbf{(I\text{-}A)S_A(I\text{-}A)^T} \quad (16)$$

As a demonstration, we compare the GOSAT based emissions to the inventories both directly (uncertainties from Equation 16) and after applying the inversion operator (e.g. see Figures 2-4).

Use of Prior Swapping to evaluate emissions: Equation 3 represents an alternative but equivalent approach for mitigating smoothing error when comparing atmospheric based emissions estimates to an inventory. After "swapping" the prior used for the GOSAT based emissions estimate with the inventory the new estimate has the following form:

$$\hat{\mathbf{z}}_{\mathbf{GOSAT\_New}} = \mathbf{z_I} + \mathbf{A}(\mathbf{z_{True}} - \mathbf{z_I}) + \boldsymbol{\delta}_n + \boldsymbol{\delta}_m \quad (17)$$

In this instance we want to take the expectation of the difference of $\hat{\mathbf{z}}_{\mathbf{GOSAT\_New}}$ and $\mathbf{z_I}$ as Equation (3) is equivalent to using $\mathbf{z_I}$ as the *a priori* in the inversion described by Equation 1:

$$\hat{\mathbf{z}}_{\mathbf{GOSAT\_New}} - \mathbf{z_I} = \mathbf{A}(\mathbf{z_{True}} - \mathbf{z_I}) = \mathbf{A}(\boldsymbol{\delta}_\mathbf{I}) + \boldsymbol{\delta}_\mathbf{n} + \boldsymbol{\delta}_\mathbf{m} \quad (18)$$

Equation 18 is the same as Equation 14 which demonstrates that the covariances as described by Equation 15 (and hence uncertainties) are the same using prior swapping or an inversion operator approach.

Appendix C: Description of Inventories

(EPA GHGI) The U.S. Environmental Protection Agency's (EPA) Inventory of U.S. Greenhouse Gas Emissions and Sinks (GHGI) provides annual estimates of methane emissions from anthropogenic sources. The gridded inventory used here covers emissions from sectors such as agriculture, energy, waste, and coal for the years 2012 to 2018 (Maasakkers et al. 2023). Desai et al. (2026) provides updated national-scale inventory estimates for 1990–2024 that are methodologically consistent with the EPA GHGI, allowing a comparable gridded product to be developed and evaluated against satellite-based inversions using the benchmark framework applied here.

1. **Total Methane Emissions**: Gridded GHGI reports U.S. CONUS methane emissions in 2015 at **23.7 Tg** of CH_4, which accounts for approximately **7% of global anthropogenic methane emissions**.

2. **Sectoral Breakdown**: The Gridded GHGI includes methane emissions of 26 individual sectors. The largest sources are (see Table 2):

    - **Livestock and Rice**: Emissions from enteric fermentation and manure management constitute a significant portion of methane emissions from this sector (8.8), with total agricultural emissions reaching **9.4 Tg** in 2018.
    - **Oil and Gas**: Methane emissions from the oil and gas sectors, including production & exploration, refining, transmission & storage, processing, and distribution, account for approximately **6.9 Tg**.

- **Waste**: Emissions from municipal solid waste (MSW) landfills, industrial landfills, wastewater treatment, and composting contributed to about **4.8 Tg**.
- **Coal Mines**: Methane from coal mining, including both active and abandoned mines, contributed approximately **2.5 Tg**.

3. **Methodology**: The GHGI combines activity data with emission factors to estimate methane emissions. The inventory uses data from sources such as the EPA's Greenhouse Gas Reporting Program (GHGRP) and U.S. Department of Agriculture (USDA). The gridded GHGI uses facility-level data as well as proxy data for sources with limited spatial information. to spatially and temporally disaggregate emissions

4. **Uncertainty and Adjustments**: The uncertainty in methane emissions is accounted for with confidence intervals provided in the GHGI report. Recent updates to the GHGI methodology include the inclusion of large well blowouts and emissions from abandoned oil and gas wells, which had not been considered in previous iterations. The inventory is continuously updated to reduce uncertainties and improve accuracy.

5. **Comparisons with Atmospheric Data**: The Gridded GHGI serves as a critical input for atmospheric inversions and can be compared with top-down estimates from satellite-based data, such as those from GOSAT.

(**EDGAR 2024**) The Emissions Database for Global Atmospheric Research

The EDGAR series of inventories provides gridded (0.1x0.1 degree) emissions of the key anthropogenic emissions contributing to the global methane budget. We refer the reader to Crippa et al. (2020, 2024) for a description of this inventory. Emissions are generated by downscaling national totals by sector using spatial proxies and projected to the 0.1 x 0.1 grid. In order to improve the accuracy of comparisons between the EDGAR inventory and the GOSAT-based fluxes, we regrid their sub-categories to livestock, waste, coal, gas, oil, and rice (e.g. see Figure 1 for the EDGAR 2024 oil&gas emissions).

(**NOAA FOG**) The NOAA fuel-based oil and gas (FOG) inventory provides oil and gas emissions for the contiguous United States (CONUS) gridded at 4km x 4km and are then regridded to (0.1 x 0.1 degree) for this work (Francoeur et al. 2021). The NOAA FOG methane emissions inventory is generated through a hybrid approach that combines activity data with atmospheric measurements to provide a more comprehensive and accurate assessment of methane emissions from the oil and gas sector. FOG combines combustion activity of drilling and production engines with fuel-based nitrogen oxides (NO_x) emission factors from measurements and empirical models (Gorchov-Negron *et al*. 2018). The activity-based NO_x emissions have been evaluated with airborne NOAA WP-3 measurements over a comprehensive number of US oil and gas basins during the Southeast Nexus Study (https://csl.noaa.gov/projects/senex/) and Shale Oil and Natural Gas Nexus Study (https://csl.noaa.gov/projects/songnex/), as well as with spaceborne observations (Dix *et al*. 2020, 2022). Oil and gas methane emissions are then inferred by tracer-tracer ratios observed by the aircraft relative to NO_x analyzed for each oil and gas basin measured (Francouer *et al*. 2021). The hybrid approach in principle allows for a better representation of emissions compared to traditional activity-based inventories as the atmospheric data likely better captures the effect of **fugitive emissions** and other hard-to-measure sources that are often underrepresented in other activity based inventory methods. Additionally, atmospheric measurements help to address uncertainties by cross-referencing emission estimates with observed methane concentrations, thus improving the overall reliability of the inventory.

Key findings from the FOG inventory include:

1. **Methane Emissions**: The FOG inventory estimates total methane emissions from oil and natural gas production **at 14.1 ± 2.0 Tg CH_4/yr for** 2015.

2. **Sectoral Breakdown**: The FOG inventory includes methane emissions from drilling, production, gathering, and processing activities. The contribution of methane emissions from the production and drilling phases is particularly significant, comprising about **60% of total methane emissions** during the oil and gas production process.

3. **Uncertainty and Evaluation**: The methane estimates from the FOG inventory are supported by aircraft-derived "top-down" emission measurements, which help

validate the inventory's accuracy. Uncertainties are evaluated through a Monte-Carlo analysis of the NOx emissions and emissions factors (Francoeur *et al*. 2021)

Code Availability

The code for the sectoral attribution is available here (Worden and Pandey, 2025): https://doi.org/10.5281/zenodo.15786798].

A Python notebook demonstrating the benchmarking approach with the GOSAT inversion fluxes is available at Pandey, S., & Worden, J. (2025). Evaluation of Methane Emissions Inventory Using Satellite Flux Inversions Data set https://doi.org/10.5281/zenodo.16921536 (Pandey and Worden, 2025)

Data Availability

GOSAT-based fluxes and emissions by sector are also available on Zenodo: https://zenodo.org/records/15786798. (Worden and Pandey, 2025)

Author Contributions

JW designed the study, performed sectoral attribution, and wrote the paper draft SP performed the inventory comparison analysis, made the figures and supported the paper writing. HN, JDM, and KB supported the analysis and paper writing. CH and CL supported the FOG analysis. DG and LS supported interpretation of the inventories. DJ, LE, DV, JE, and ZQ produced the GOSAT fluxes, supported the interpretation, and reviewed the paper.

Competing Interests: The authors declare that to their knowledge there are no competing interests.

Acknowledgements

Part of this research was carried out at the Jet Propulsion Laboratory, California Institute of Technology, under a contract with the National Aeronautics and Space Administration. Chatgpt used to support paper editing.

Financial Support

This work is funded by the NASA Carbon Monitoring System (Carbon Monitoring System NNH23ZDA001N-CMS) and through the NASA Greenhouse Gas Center.

References

Alvarez, R. A., Zavala-Araiza, D., Lyon, D. R., Allen, D. T., Barkley, Z. R., Brandt, A. R., Davis, K. J., Herndon, S. C., Jacob, D. J., Karion, A., Kort, E. A., Lamb, B. K., Lauvaux, T., Maasakkers, J. D., Marchese, A. J., Omara, M., Pacala, S. W., Peischl, J., Robinson, A. L., Shepson, P. B., Sweeney, C., Townsend-Small, A., Wofsy, S. C., and Hamburg, S. P.: Assessment of methane emissions from the U.S. oil and gas supply chain, Science, 361, eaar7204, https://doi.org/10.1126/science.aar7204, 2018.

Barkley, Z. R., Davis, K. J., Miles, N. L., Richardson, S. J., Deng, A., Hmiel, B., Lyon, D. R., and Lauvaux, T.: Quantification of oil and gas methane emissions in the Delaware and Marcellus basins using a network of continuous tower-based measurements, Atmos. Chem. Phys., 23, 6127-6144, https://doi.org/10.5194/acp-23-6127-2023, 2023.

Bowman, K. W., Rodgers, C. D., Kulawik, S. S., Worden, J., Sarkissian, E., Osterman, G., Steck, T., Lou, M., Eldering, A., Shephard, M., Worden, H., Lampel, M., Clough, S., Brown, P., Rinsland, C., Gunson, M., and Beer, R.: Tropospheric emission spectrometer: retrieval method and error analysis, IEEE T. Geosci. Remote, 44, 1297-1307, https://doi.org/10.1109/TGRS.2006.871234, 2006.

Crippa, M., Solazzo, E., Huang, G., Guizzardi, D., Koffi, E., Muntean, M., Schieberle, C., Friedrich, R., and Janssens-Maenhout, G.: High resolution temporal profiles in the Emissions Database for Global Atmospheric Research, Sci. Data, 7, 121, https://doi.org/10.1038/s41597-020-0462-2, 2020.

Crippa, M., Guizzardi, D., Pagani, F., Schiavina, M., Melchiorri, M., Pisoni, E., Graziosi, F., Muntean, M., Maes, J., Dijkstra, L., van Damme, M., Clarisse, L., and Coheur, P.: Insights into the spatial distribution of global, national, and subnational greenhouse gas emissions in the Emissions Database for Global Atmospheric Research (EDGAR v8.0), Earth Syst. Sci. Data, 16, 2811-2830, https://doi.org/10.5194/essd-16-2811-2024, 2024.

Crippa, M., Guizzardi, D., Pagani, F., Banja, M., Muntean, M., Schaaf, E., Monforti-Ferrario, F., Becker, W., Quadrelli, R., Risquez Martin, A., Taghavi-Moharamli, P., Koeykkae, J., Grassi, G., Rossi, S., Melo, J., Oom, D., Branco, A., San-Miguel, J., Manca, G., Pisoni, E., Vignati, E., and Pekar, F.: GHG emissions of all world countries, Publications Office of the European Union, Luxembourg, https://doi.org/10.2760/4002897, 2024.

Cusworth, D. H., Duren, R. M., Thorpe, A. K., Tseng, E., Thompson, D., Guha, A., Newman, S., Foster, K. T., and Miller, C. E.: Using remote sensing to detect, validate, and quantify methane emissions from California solid waste operations, Environ. Res. Lett., 15, 054012, https://doi.org/10.1088/1748-9326/ab7b99, 2020.

Cusworth, D. H., Bloom, A. A., Ma, S., Miller, C. E., Bowman, K., Yin, Y., Maasakkers, J. D., Zhang, Y., Scarpelli, T. R., Qu, Z., Jacob, D. J., and Worden, J. R.: A Bayesian framework for deriving sector-based methane emissions from top-down fluxes, Commun. Earth Environ., 2, 242, https://doi.org/10.1038/s43247-021-00312-6, 2021.

Cusworth, D. H., Thorpe, A. K., Ayasse, A. K., Stepp, D., Heckler, J., Asner, G. P., Miller, C. E., Yadav, V., Chapman, J. W., Eastwood, M. L., Green, R. O., Hmiel, B., Lyon, D. R., and Duren, R. M.: Strong methane point sources contribute a disproportionate fraction of total emissions across multiple basins in the United States, Proc. Natl. Acad. Sci. USA, 119, e2202338119, https://doi.org/10.1073/pnas.2202338119, 2022.

Cusworth, D. H., Duren, R. M., Ayasse, A. K., Jiorle, R., Howell, K., Aubrey, A., Green, R. O., Eastwood, M. L., Chapman, J. W., Thorpe, A. K., Heckler, J., Asner, G. P., Smith, M. L., Thoma, E., Krause, M. J., Heins, D., and Thorneloe, S.: Quantifying methane emissions from United States landfills, Science, 383, 1499-1504, https://doi.org/10.1126/science.adi7735, 2024.

Desai, M., Camobreco, V., Hedger, T., Irving, W., Rewcastle, K., Steller, J., Barbieri, L., Weitz, M., Murumkar, T., Fawcett, A., Lou, J., Cui, R., and Hultman, N.: Greenhouse Gas Inventory and Analysis for the United States: 1990-2024, Center for Global Sustainability, University of Maryland, College Park, available at: https://drum.lib.umd.edu/items/8a22e947-e7c1-4273-b831-0d4cbf294aba, 2026.

Dix, B., de Bruin, J., Roosenbrand, E., Vlemmix, T., Francoeur, C., Gorchov-Negron, A. M., McDonald, B., Zhizhin, M., Elvidge, C., Veefkind, P., Levelt, P., and de Gouw, J. A.: Nitrogen oxide emissions from U.S. oil and gas production: recent trends and source attribution, Geophys. Res. Lett., 47, e2019GL085866, https://doi.org/10.1029/2019GL085866, 2020.

Dix, B., Francoeur, C., Li, M., Serrano-Calvo, R., Levelt, P. F., Veefkind, J. P., McDonald, B. C., and de Gouw, J. A.: Quantifying NOx emissions from U.S. oil and gas production regions using TROPOMI NO2, ACS Earth Space Chem., 6, 403-414, https://doi.org/10.1021/acsearthspacechem.1c00387, 2022.

East, J. D., Jacob, D. J., Jervis, D., Balasus, N., Estrada, L. A., Hancock, S. E., Sulprizio, M. P., Thomas, J., Wang, X., Chen, Z., Varon, D. J., and Worden, J. R.: Worldwide inference of national methane emissions by inversion of satellite observations with UNFCCC prior estimates, Nat. Commun., 16, 11004, https://doi.org/10.1038/s41467-025-67122-8, 2025.

EDGAR: EDGAR Community GHG Database, a collaboration between the European Commission, Joint Research Centre (JRC), and the International Energy Agency (IEA), including IEA-EDGAR CO2, EDGAR CH4, EDGAR N2O, and EDGAR F-gases version 2024, European Commission, Joint Research Centre, available at: https://edgar.jrc.ec.europa.eu/dataset_ghg2024, last access: 1 October 2025, 2024.

EPA: Fact Sheet on Mandatory Reporting of Greenhouse Gases (40 CFR Part 98), U.S. Environmental Protection Agency, available at: https://www.epa.gov/sites/default/files/2015-07/documents/part98factsheet.pdf, 2011.

EPA: Inventory of U.S. Greenhouse Gas Emissions and Sinks: 1990-2021, U.S. Environmental Protection Agency, EPA 430-R-23-002, available at:

https://www.epa.gov/ghgemissions/inventory-us-greenhouse-gas-emissions-and-sinks-1990-2021, 2023.

Etiope, G., Ciotoli, G., Schwietzke, S., and Schoell, M.: Gridded maps of geological methane emissions and their isotopic signature, Earth Syst. Sci. Data, 11, 1-22, https://doi.org/10.5194/essd-11-1-2019, 2019. [If cited in text as Etiope et al. (2018), update the in-text citation to 2019.]

Francoeur, C. B., McDonald, B. C., Gilman, J. B., Zarzana, K. J., Dix, B., Brown, S. S., de Gouw, J. A., Frost, G. J., Li, M., McKeen, S. A., Peischl, J., Pollack, I. B., Ryerson, T. B., Thompson, C., Warneke, C., and Trainer, M.: Quantifying methane and ozone precursor emissions from oil and gas production regions across the contiguous US, Environ. Sci. Technol., 55, 9129-9139, https://doi.org/10.1021/acs.est.0c07352, 2021.

Gorchov-Negron, A. M., McDonald, B. C., McKeen, S. A., Peischl, J., Ahmadov, R., de Gouw, J. A., Frost, G. J., Hastings, M. G., Pollack, I. B., Ryerson, T. B., Thompson, C., Warneke, C., and Trainer, M.: Development of a fuel-based oil and gas inventory of nitrogen oxides emissions, Environ. Sci. Technol., 52, 10175-10185, https://doi.org/10.1021/acs.est.8b02245, 2018.

Gordon, D.: No Standard Oil: Managing Abundant Petroleum in a Warming World, paperback edn., Oxford University Press, Oxford, ISBN 9780197832165, 2025.

Hancock, S. E., Jacob, D. J., Chen, Z., Nesser, H., Davitt, A., Varon, D. J., Sulprizio, M. P., Balasus, N., Estrada, L. A., East, J. D., Penn, E., Randles, C. A., Worden, J., Aben, I., Parker, R. J., and Maasakkers, J. D.: Satellite quantification of methane emissions from South American countries: a high-resolution inversion of TROPOMI and GOSAT observations, Atmos. Chem. Phys., 25, 797-833, https://doi.org/10.5194/acp-25-797-2025, 2025.

Herman, R. L., Cherry, J. E., Young, J., Welker, J. M., Noone, D., Kulawik, S. S., and Worden, J.: Aircraft validation of Aura Tropospheric Emission Spectrometer retrievals of HDO/H2O, Atmos. Meas. Tech., 7, 3127-3138, https://doi.org/10.5194/amt-7-3127-2014, 2014.

Hmiel, B., Petrenko, V. V., Dyonisius, M. N., Buizert, C., Smith, A. M., Place, P. F., Harth, C., Beaudette, R., Hua, Q., Yang, B., Vimont, I., Michel, S. E., Severinghaus, J. P., Etheridge, D., Bromley, T., Schmitt, J., Fain, X., Weiss, R. F., and Dlugokencky, E.: Preindustrial 14CH4 indicates greater anthropogenic fossil CH4 emissions, Nature, 578, 409-412, https://doi.org/10.1038/s41586-020-1991-8, 2020.

Hristov, A. N., Harper, M., Meinen, R., Day, R., Lopes, J., Ott, T., Venkatesh, A., and Randles, C. A.: Discrepancies and uncertainties in bottom-up gridded inventories of livestock methane emissions for the contiguous United States, Environ. Sci. Technol., 51, 13668-13677, https://doi.org/10.1021/acs.est.7b03332, 2017.

IEA: Global Methane Tracker 2025, International Energy Agency, available at: https://www.iea.org/reports/global-methane-tracker-2025, 2025.

Jacob, D. J., Varon, D. J., Cusworth, D. H., Dennison, P. E., Frankenberg, C., Gautam, R., Guanter, L., Kelley, J., McKeever, J., Ott, L. E., Poulter, B., Qu, Z., Thorpe, A. K., Worden, J. R., and Duren, R. M.: Quantifying methane emissions from the global scale down to point sources using satellite observations of atmospheric methane, Atmos. Chem. Phys., 22, 9617-9646, https://doi.org/10.5194/acp-22-9617-2022, 2022.

Janardanan, R., Maksyutov, S., Wang, F., Nayagam, L., Sahu, S. K., Mangaraj, P., Saunois, M., Lan, X., and Matsunaga, T.: Country-level methane emissions and their sectoral trends during 2009-2020 estimated by high-resolution inversion of GOSAT and surface observations, Environ. Res. Lett., 19, 034007, https://doi.org/10.1088/1748-9326/ad2436, 2024.

Jiang, Z., Jones, D. B. A., Worden, H. M., Deeter, M. N., Henze, D. K., Worden, J., Bowman, K. W., Brenninkmeijer, C. A. M., and Schuck, T. J.: Impact of model errors in convective transport on CO source estimates inferred from MOPITT CO retrievals, J. Geophys. Res.-Atmos., 118, 2073-2083, https://doi.org/10.1002/jgrd.50216, 2013.

Kort, E. A., Eluszkiewicz, J., Stephens, B. B., Miller, J. B., Gerbig, C., Nehrkorn, T., Daube, B. C., Kaplan, J. O., Houweling, S., and Wofsy, S. C.: Emissions of CH4 and N2O over the United States and Canada based on a receptor-oriented modeling framework and COBRA-NA atmospheric observations, Geophys. Res. Lett., 35, L18808, https://doi.org/10.1029/2008GL034031, 2008.

Kruskamp, N., Lohman, H., Burnette, A., Coxen, C., Ellermeier, N., Bollenbacher, J., Powers, J., Coffield, S., Farhat, Y., and Maasakkers, J.: Gridded U.S. Anthropogenic Methane Greenhouse Gas Inventory (gridded GHGI), Zenodo [data set], https://doi.org/10.5281/zenodo.16782735, 2025.

Lu, X., Jacob, D. J., Zhang, Y., Shen, L., Sulprizio, M. P., Maasakkers, J. D., Varon, D. J., Qu, Z., Chen, Z., Hmiel, B., Parker, R. J., Boesch, H., Wang, H., He, C., and Fan, S.: Observation-derived 2010-2019 trends in methane emissions and intensities from U.S. oil and gas fields tied to activity metrics, Proc. Natl. Acad. Sci. USA, 120, e2217900120, https://doi.org/10.1073/pnas.2217900120, 2023.

Maasakkers, J. D., Jacob, D. J., Sulprizio, M. P., Turner, A. J., Weitz, M., Wirth, T., Hight, C., DeFigueiredo, M., Desai, M., Schmeltz, R., Hockstad, L., Bloom, A. A., Bowman, K. W., Jeong, S., and Fischer, M. L.: Gridded national inventory of U.S. methane emissions, Environ. Sci. Technol., 50, 13123-13133, https://doi.org/10.1021/acs.est.6b02878, 2016.

Maasakkers, J. D., Jacob, D. J., Sulprizio, M. P., Scarpelli, T. R., Nesser, H., Sheng, J.-X., Zhang, Y., Hersher, M., Bloom, A. A., Bowman, K. W., Worden, J. R., Janssens-Maenhout, G., and Parker, R. J.: Global distribution of methane emissions, emission trends, and OH concentrations and trends inferred from an inversion of GOSAT satellite data for 2010–2015, Atmos. Chem. Phys., 19, 7859–7881, https://doi.org/10.5194/acp-19-7859-2019, 2019.

Maasakkers, J. D., Jacob, D. J., Sulprizio, M. P., Scarpelli, T. R., Nesser, H., Sheng, J., Zhang, Y., Lu, X., Bloom, A. A., Bowman, K. W., Worden, J. R., and Parker, R. J.: 2010-2015 North American methane emissions, sectoral contributions, and trends: a high-resolution inversion of GOSAT observations of atmospheric methane, Atmos. Chem. Phys., 21, 4339-4356, https://doi.org/10.5194/acp-21-4339-2021, 2021.

Maasakkers, J. D., McDuffie, E. E., Sulprizio, M. P., Chen, C., Schultz, M., Brunelle, L., Thrush, R., Steller, J., Sherry, C., Jacob, D. J., Jeong, S., Irving, B., and Weitz, M.: A gridded inventory of annual 2012-2018 U.S. anthropogenic methane emissions, Environ. Sci. Technol., 57, 16276-16288, https://doi.org/10.1021/acs.est.3c05138, 2023.

McNorton, J. R., Bousserez, N., Agusti-Panareda, A., Balsamo, G., Choulga, M., Dawson, A., Engelen, R., Kipling, Z., and Lang, S.: Representing model uncertainty for global

atmospheric CO2 flux inversions using ECMWF-IFS-46R1, Geosci. Model Dev., 13, 2297-2313, https://doi.org/10.5194/gmd-13-2297-2020, 2020.

Miller, S. M., Wofsy, S. C., Michalak, A. M., Kort, E. A., Andrews, A. E., Biraud, S. C., Dlugokencky, E. J., Eluszkiewicz, J., Fischer, M. L., Janssens-Maenhout, G., Miller, B. R., Miller, J. B., Montzka, S. A., Nehrkorn, T., and Sweeney, C.: Anthropogenic emissions of methane in the United States, Proc. Natl. Acad. Sci. USA, 110, 20018-20022, https://doi.org/10.1073/pnas.1314392110, 2013.

Nesser, H., Jacob, D. J., Maasakkers, J. D., Lorente, A., Chen, Z., Lu, X., Shen, L., Qu, Z., Sulprizio, M. P., Winter, M., Ma, S., Bloom, A. A., Worden, J. R., Stavins, R. N., and Randles, C. A.: High-resolution U.S. methane emissions inferred from an inversion of 2019 TROPOMI satellite data: contributions from individual states, urban areas, and landfills, Atmos. Chem. Phys., 24, 5069-5091, https://doi.org/10.5194/acp-24-5069-2024, 2024.

Nisbet, E. G., Manning, M. R., Dlugokencky, E. J., Fisher, R. E., Lowry, D., Michel, S. E., Myhre, C. L., Platt, S. M., Allen, G., Bousquet, P., Brownlow, R., Cain, M., France, J. L., Hermansen, O., Hossaini, R., Jones, A. E., Levin, I., Manning, A. C., Myhre, G., Pyle, J. A., Vaughn, B. H., Warwick, N. J., and White, J. W. C.: Very strong atmospheric methane growth in the 4 years 2014-2017: implications for the Paris Agreement, Global Biogeochem. Cy., 33, 318-342, https://doi.org/10.1029/2018GB006009, 2019.

Pandey, S., Worden, J., Cusworth, D. H., Varon, D. J., Thill, M. D., Jacob, D. J., and Bowman, K. W.: Relating multi-scale plume detection and area estimates of methane emissions: a theoretical and empirical analysis, Environ. Sci. Technol., 59, 7931-7947, https://doi.org/10.1021/acs.est.4c07415, 2025.

Pandey, S. and Worden, J.: Evaluation of Methane Emissions Inventory Using Satellite Flux Inversions, Zenodo [code and data set], https://doi.org/10.5281/zenodo.16921536, 2025.

Parker, R., Boesch, H., Cogan, A., Fraser, A., Feng, L., Palmer, P. I., Messerschmidt, J., Deutscher, N., Griffith, D. W. T., Notholt, J., Wennberg, P. O., and Wunch, D.: Methane observations from the Greenhouse Gases Observing SATellite: comparison to ground-based TCCON data and model calculations, Geophys. Res. Lett., 38, L15807, https://doi.org/10.1029/2011GL047871, 2011.

Petrescu, A. M. R., Peters, G. P., Engelen, R., Houweling, S., Brunner, D., Tsuruta, A., Matthews, B., Patra, P. K., Belikov, D., Thompson, R. L., Hoeglund-Isaksson, L., Zhang, W., Segers, A. J., Etiope, G., Ciotoli, G., Peylin, P., Chevallier, F., Aalto, T., Andrew, R. M., Bastviken, D., Berchet, A., Broquet, G., Conchedda, G., Dellaert, S. N. C., van der Gon, H. D., Guetschow, J., Haussaire, J.-M., Lauerwald, R., Markkanen, T., van Peet, J. C. A., Pison, I., Regnier, P., Solum, E., Scholze, M., Tenkanen, M., Tubiello, F. N., van der Werf, G. R., and Worden, J. R.: Comparison of observation- and inventory-based methane emissions for eight large global emitters, Earth Syst. Sci. Data, 16, 4325-4350, https://doi.org/10.5194/essd-16-4325-2024, 2024.

Qu, Z., Jacob, D. J., Zhang, Y., Shen, L., Varon, D. J., Lu, X., Scarpelli, T., Bloom, A., Worden, J., and Parker, R. J.: Attribution of the 2020 surge in atmospheric methane by inverse analysis of GOSAT observations, Environ. Res. Lett., 17, 094003, https://doi.org/10.1088/1748-9326/ac8754, 2022.

Qu, Z., Jacob, D. J., Bloom, A. A., Worden, J. R., Parker, R. J., and Boesch, H.: Inverse modeling of 2010-2022 satellite observations shows that inundation of the wet tropics drove the 2020-2022 methane surge, Proc. Natl. Acad. Sci. USA, 121, e2402730121, https://doi.org/10.1073/pnas.2402730121, 2024.

Rodgers, C. D.: Inverse Methods for Atmospheric Sounding: Theory and Practice, World Scientific, Singapore, https://doi.org/10.1142/3171, 2000.

Rodgers, C. D. and Connor, B. J.: Intercomparison of remote sounding instruments, J. Geophys. Res.-Atmos., 108, 4116, https://doi.org/10.1029/2002JD002299, 2003.

Saunois, M., Stavert, A. R., Poulter, B., Bousquet, P., Canadell, J. G., Jackson, R. B., Raymond, P. A., Dlugokencky, E. J., Houweling, S., Patra, P. K., Ciais, P., Arora, V. K., Bastviken, D., Bergamaschi, P., Blake, D. R., Brailsford, G., Bruhwiler, L., Carlson, K. M., Carroll, M., Castaldi, S., Chandra, N., Crevoisier, C., Crill, P. M., Covey, K., Curry, C. L., Etiope, G., Frankenberg, C., Gedney, N., Hegglin, M. I., Hoeglund-Isaksson, L., Hugelius, G., Ishizawa, M., Ito, A., Janssens-Maenhout, G., Jensen, K. M., Joos, F., Kleinen, T., Krummel, P. B., Langenfelds, R. L., Laruelle, G. G., Liu, L., Machida, T., Maksyutov, S., McDonald, K. C., McNorton, J., Miller, P. A., Melton, J. R., Morino, I., Mueller, J., Murguia-Flores, F., Naik, V., Niwa, Y., Noce, S., O'Doherty, S., Parker, R. J., Peng, C., Peng, S., Peters, G. P., Prigent, C., Prinn, R., Ramonet, M., Regnier, P., Riley, W. J., Rosentreter, J. A., Segers, A., Simpson, I. J., Shi, H., Smith, S. J., Steele, L. P., Thornton, B. F., Tian, H., Tohjima, Y., Tubiello, F. N., Tsuruta, A., Viovy, N., Voulgarakis, A., van Weele, M., van der Werf, G. R., Weiss, R. F., Worthy, D., Wunch, D., Yin, Y., Yoshida, Y., Zhang, W., Zhang, Z., Zhao, Y., Zheng, B., Zhu, Q., Zhu, Q., and Zhuang, Q.: The global methane budget 2000-2017, Earth Syst. Sci. Data, 12, 1561-1623, https://doi.org/10.5194/essd-12-1561-2020, 2020.

Schuh, A. E., Jacobson, A. R., Basu, S., Weir, B., Baker, D., Bowman, K., Chevallier, F., Crowell, S., Davis, K. J., Deng, F., Denning, S., Feng, L., Jones, D., Liu, J., and Palmer, P. I.: Quantifying the impact of atmospheric transport uncertainty on CO2 surface flux estimates, Global Biogeochem. Cy., 33, 484-500, https://doi.org/10.1029/2018GB006086, 2019.

Sherwin, E. D., Rutherford, J. S., Zhang, Z., Chen, Y., Wetherley, E. B., Yakovlev, P. V., Berman, E. S. F., Jones, B. B., Cusworth, D. H., Thorpe, A. K., Ayasse, A. K., Duren, R. M., and Brandt, A. R.: U.S. oil and gas system emissions from nearly one million aerial site measurements, Nature, 627, 328-334, https://doi.org/10.1038/s41586-024-07117-5, 2024.

Wecht, K. J., Jacob, D. J., Sulprizio, M. P., Santoni, G. W., Wofsy, S. C., Parker, R., Boesch, H., and Worden, J.: Spatially resolving methane emissions in California: constraints from the CalNex aircraft campaign and from present (GOSAT, TES) and future (TROPOMI, geostationary) satellite observations, Atmos. Chem. Phys., 14, 8173-8184, https://doi.org/10.5194/acp-14-8173-2014, 2014.

Wolf, J., Asrar, G. R., and West, T. O.: Revised methane emissions factors and spatially distributed annual carbon fluxes for global livestock, Carbon Balance Manage., 12, 16, https://doi.org/10.1186/s13021-017-0084-y, 2017.

Worden, J., Kulawik, S. S., Shephard, M. W., Clough, S. A., Worden, H., Bowman, K., and Goldman, A.: Predicted errors of tropospheric emission spectrometer nadir retrievals from spectral window selection, J. Geophys. Res.-Atmos., 109, D09308, https://doi.org/10.1029/2004JD004522, 2004.

966 Worden, J. R., Cusworth, D. H., Qu, Z., Yin, Y., Zhang, Y., Bloom, A. A., Ma, S., Byrne, B. K.,
967 Scarpelli, T., Maasakkers, J. D., Crisp, D., Duren, R., and Jacob, D. J.: The 2019 methane
968 budget and uncertainties at 1 degree resolution and each country through Bayesian
969 integration of GOSAT total column methane data and a priori inventory estimates, Atmos.
970 Chem. Phys., 22, 6811-6841, https://doi.org/10.5194/acp-22-6811-2022, 2022.

971 Worden, J. R., Pandey, S., Zhang, Y., Cusworth, D. H., Qu, Z., Bloom, A. A., Ma, S.,
972 Maasakkers, J. D., Byrne, B., Duren, R., Crisp, D., Gordon, D., and Jacob, D. J.: Verifying
973 methane inventories and trends with atmospheric methane data, AGU Adv., 4,
974 e2023AV000871, https://doi.org/10.1029/2023AV000871, 2023.

975 Worden, J. R. and Pandey, S.: Evaluation of Methane Emissions Inventory Using Satellite Flux
976 Inversions, Zenodo [data set], https://doi.org/10.5281/zenodo.15786798, 2025.

977 World Bank: Global Gas Flaring Tracker Report, July 2025, World Bank, Washington, DC,
978 available at: https://thedocs.worldbank.org/en/doc/bd2432bbb0e514986f382f61b14b2608-
979 0400072025/original/Global-Gas-Flaring-Tracker-Report-July-2025.pdf, 2025.

980 Zavala-Araiza, D., Lyon, D. R., Alvarez, R. A., Davis, K. J., Harriss, R., Herndon, S. C., Karion,
981 A., Kort, E. A., Lamb, B. K., Lan, X., Marchese, A. J., Pacala, S. W., Robinson, A. L.,
982 Shepson, P. B., Sweeney, C., Talbot, R., Townsend-Small, A., Yacovitch, T. I., Zimmerle, D.
983 J., and Hamburg, S. P.: Reconciling divergent estimates of oil and gas methane emissions,
984 Proc. Natl. Acad. Sci. USA, 112, 15597-15602, https://doi.org/10.1073/pnas.1522126112,
985 2015.

986 Zhang, P., Zhang, Y., and Liang, R.: Correction of simulation biases in stratospheric methane
987 concentrations for the inverse analysis of satellite column observations, J. Geophys. Res.-
988 Atmos., 130, e2024JD042596, https://doi.org/10.1029/2024JD042596, 2025.

989 Zhang, Y., Jacob, D. J., Lu, X., Maasakkers, J. D., Scarpelli, T. R., Sheng, J.-X., Shen, L., Qu,
990 Z., Sulprizio, M. P., Chang, J., Bloom, A. A., Ma, S., Worden, J., Parker, R. J., and Boesch,
991 H.: Attribution of the accelerating increase in atmospheric methane during 2010-2018 by
992 inverse analysis of GOSAT observations, Atmos. Chem. Phys., 21, 3643-3666,
993 https://doi.org/10.5194/acp-21-3643-2021, 2021.

994

Figure Captions

Figure 1: (Top Panels) Mean Emissions for Oil and Gas for 2015 (at 1x1 degree lon/lat gridding) as calculated from the EPA, FOG, EDGAR inventories. (Bottom Panels) Differences between FOG and EPA and EDGAR and EPA.

Figure 2: Comparison of the U.S. oil and gas (O&G) methane emissions in 2015 from the GOSAT inversion with those from the FOG inventory. The upper left panel (a) shows the GOSAT based estimate. The upper right panel (b) shows the original FOG emissions. The middle left panel (c) shows the difference between the top two. The middle right panel shows the difference between FOG emissions and GOSAT based emissions after applying the inversion operator (denoted AK). All figures use 1x1 degree gridding; only differences larger than the corresponding calculated uncertainty are shown. The bottom right panel (E) shows the diagonal of the averaging kernel (or DOFS) corresponding to that location for oil and gas emissions.

Figure 3: Same as in Figure 2 but for the EDGAR inventory.

Figure 4: Same as in Figure 3 but for the EPA GHGI inventory.

Figure 5: Comparison of the integrated total oil and gas (O&G) emissions derived from GOSAT with those from the FOG, EPA GHGI , and EDGAR 2024 inventories, both with and without the inversion operator (AK) applied. Comparisons should be made between the GOSAT estimate and the inventories with inversion operator (AK) applied.

Figure 6: Integrated totals for oil and gas emissions between 2012 and 2020. The GOSAT inversion operator has been applied to the FOG, EPA GHGI , and EDGAR 2024 inventories; the biases between the comparisons are therefore not due to the prior used with the GOSAT inversion.

Figure 7: Similar to Figure 2 but for EDGAR 2024 livestock emissions

Figure 8: Similar to Figure 7 but for EPA GHGI livestock emissions

Figure 9: Comparison of the integrated livestock emissions derived from GOSAT with those from the EPA GHGI and EDGAR 2024 inventories, both with and without the inversion operator (AK) applied. Comparisons should be made between the GOSAT estimate and the inventories with inversion operator (AK) applied.

Figure 10: Integrated totals for Livestock Emissions between 2012 and 2020. The inversion operator has been applied to the inventories.

Figure 11: Similar to Figure 2 but for EDGAR 2024 waste emissions

Figure 12: Similar to Figure 3 but for EPA GHGI waste emissions

Figure 13: Integrated total methane emissions from the waste sector based on GOSAT, along with estimates from the EPA GHGI and EDGAR 2024 inventories, both with and without the inversion operator applied.

1043 Figures

1044

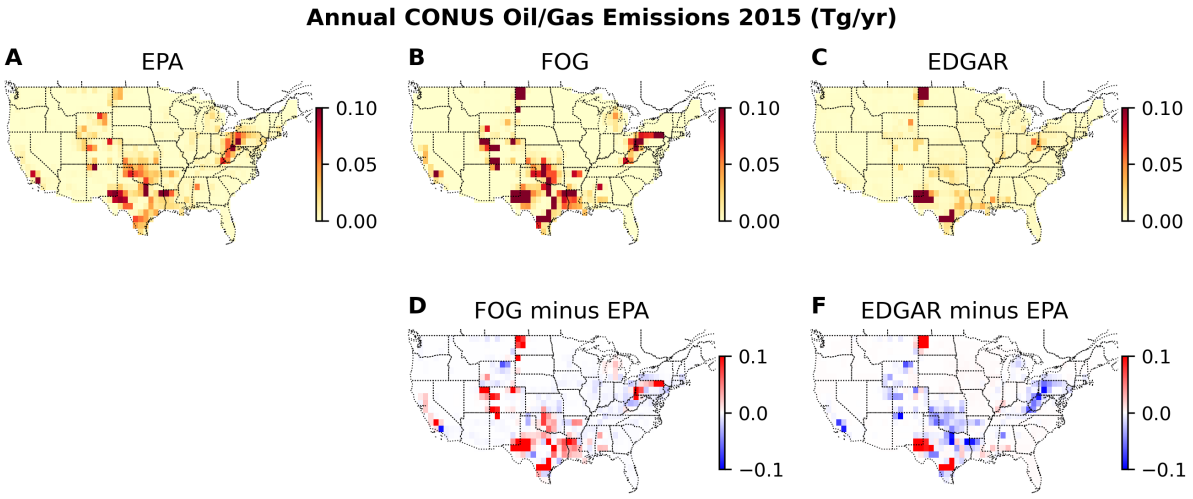

Figure 1: (Top Panels) Mean Emissions for Oil and Gas for 2015 (at 1x1 degree lon/lat gridding) as calculated from the EPA, FOG, EDGAR inventories. (Bottom Panels) Differences between FOG and EPA and EDGAR and EPA.

1045

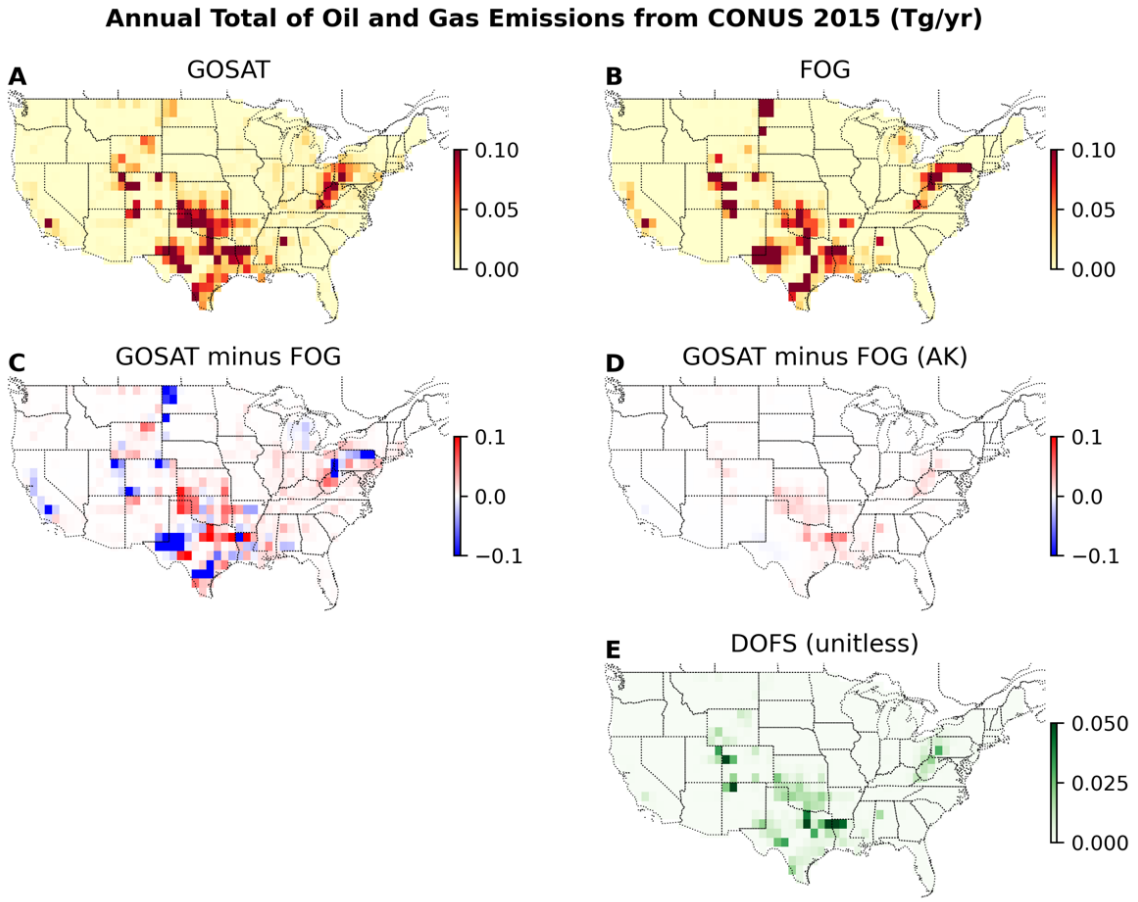

Figure 2: Comparison of the U.S. oil and gas (O&G) methane emissions in 2015 from the GOSAT inversion with those from the FOG inventory. The upper left panel (a) shows the GOSAT based estimate. The upper right panel (b) shows the original FOG emissions. The middle left panel (c) shows the difference between the top two. The middle right panel shows the difference between FOG emissions and GOSAT based emissions after applying the inversion operator (denoted AK). All figures use 1x1 degree gridding; only differences larger than the corresponding calculated uncertainty are shown. The bottom right panel (E) shows the diagonal of the averaging kernel (or DOFS) corresponding to that location for oil and gas emissions.

1046

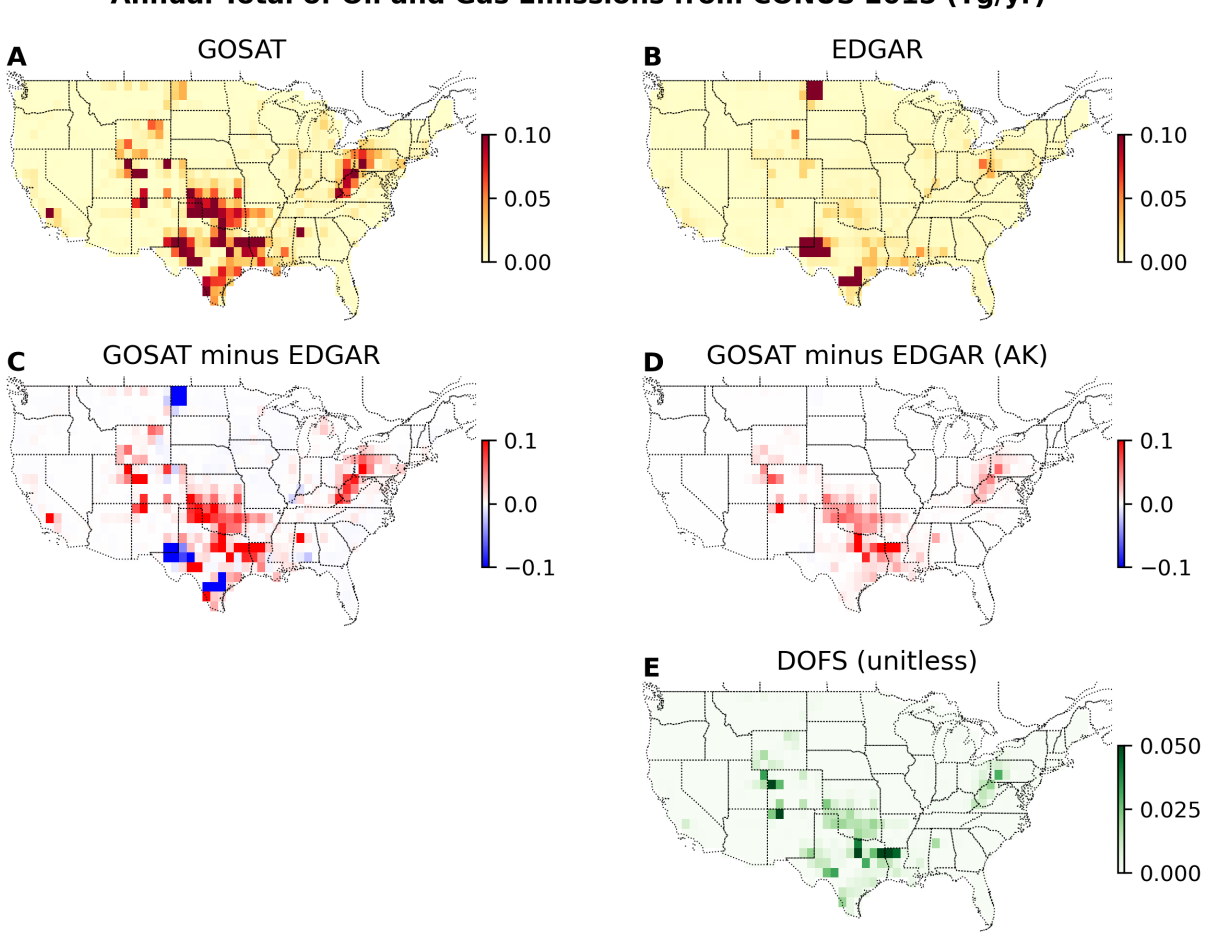

Figure 3: Same as in Figure 2 but for the EDGAR inventory.

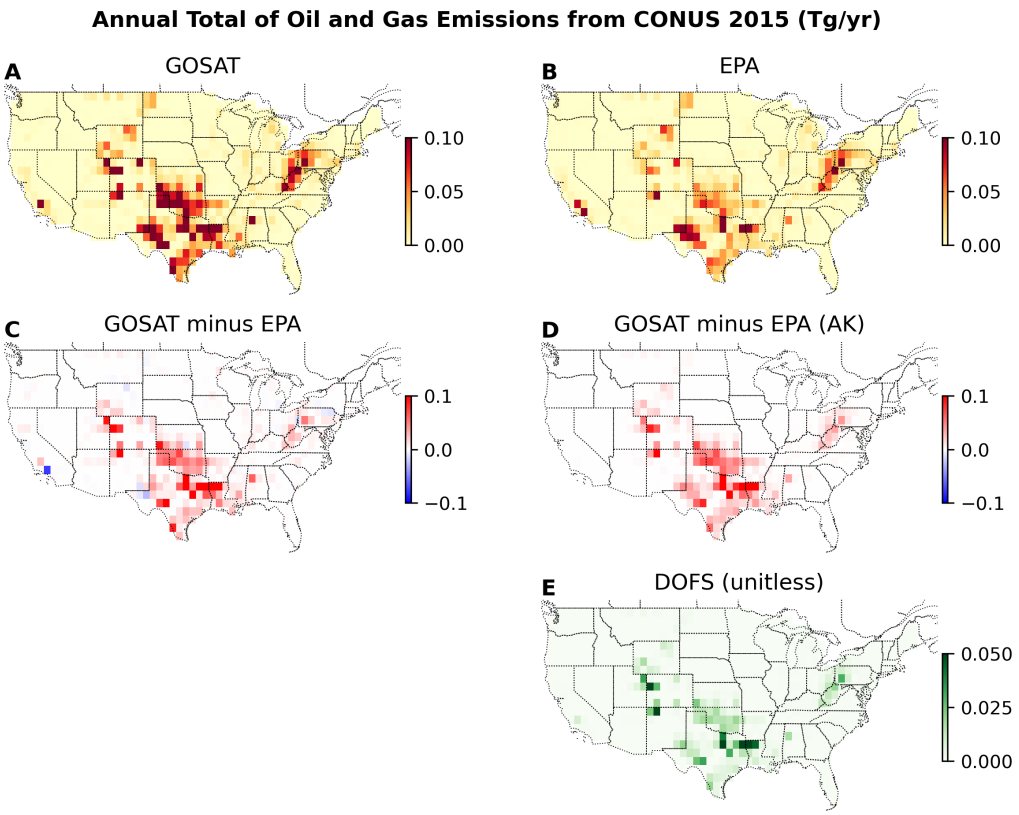

Figure 4: Same as in Figure 3 but for the EPA GHGI inventory.

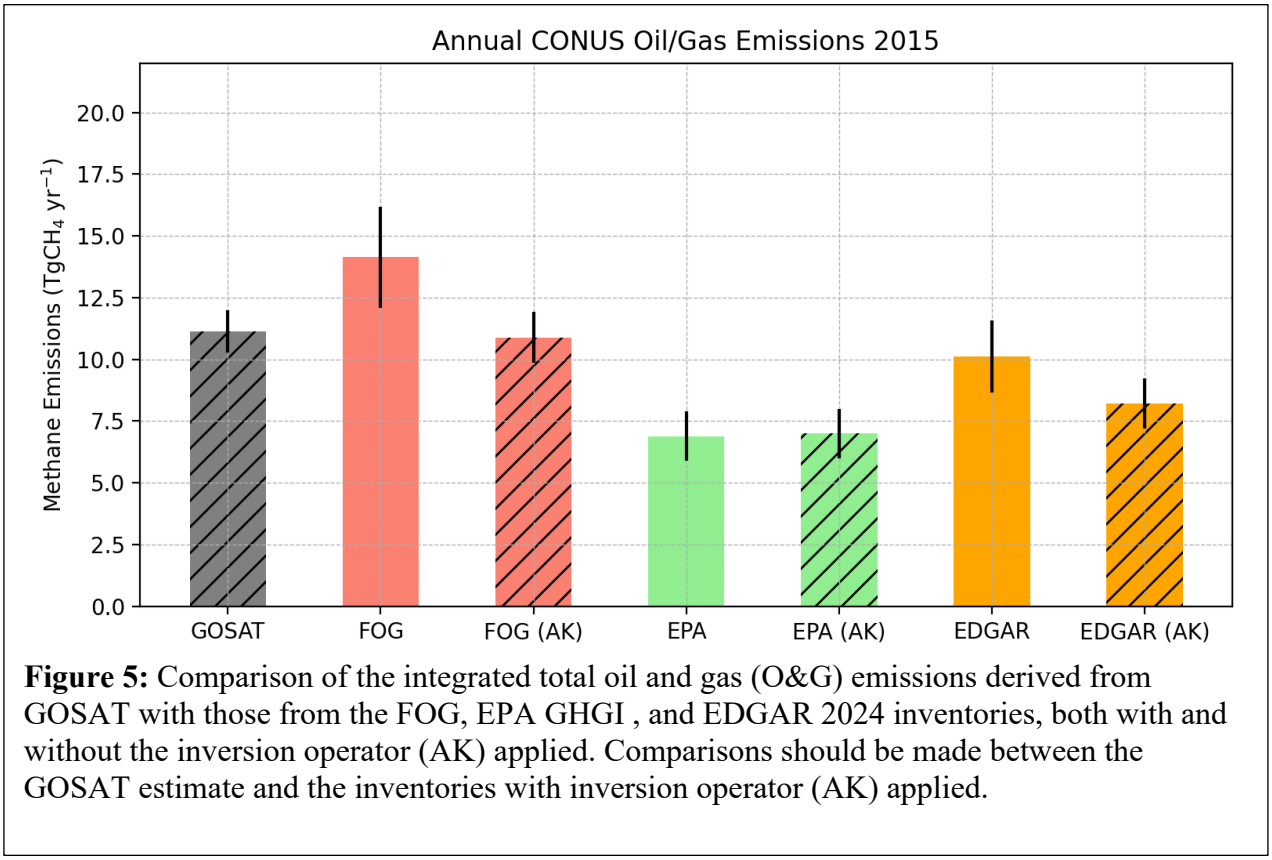

Figure 5: Comparison of the integrated total oil and gas (O&G) emissions derived from GOSAT with those from the FOG, EPA GHGI , and EDGAR 2024 inventories, both with and without the inversion operator (AK) applied. Comparisons should be made between the GOSAT estimate and the inventories with inversion operator (AK) applied.

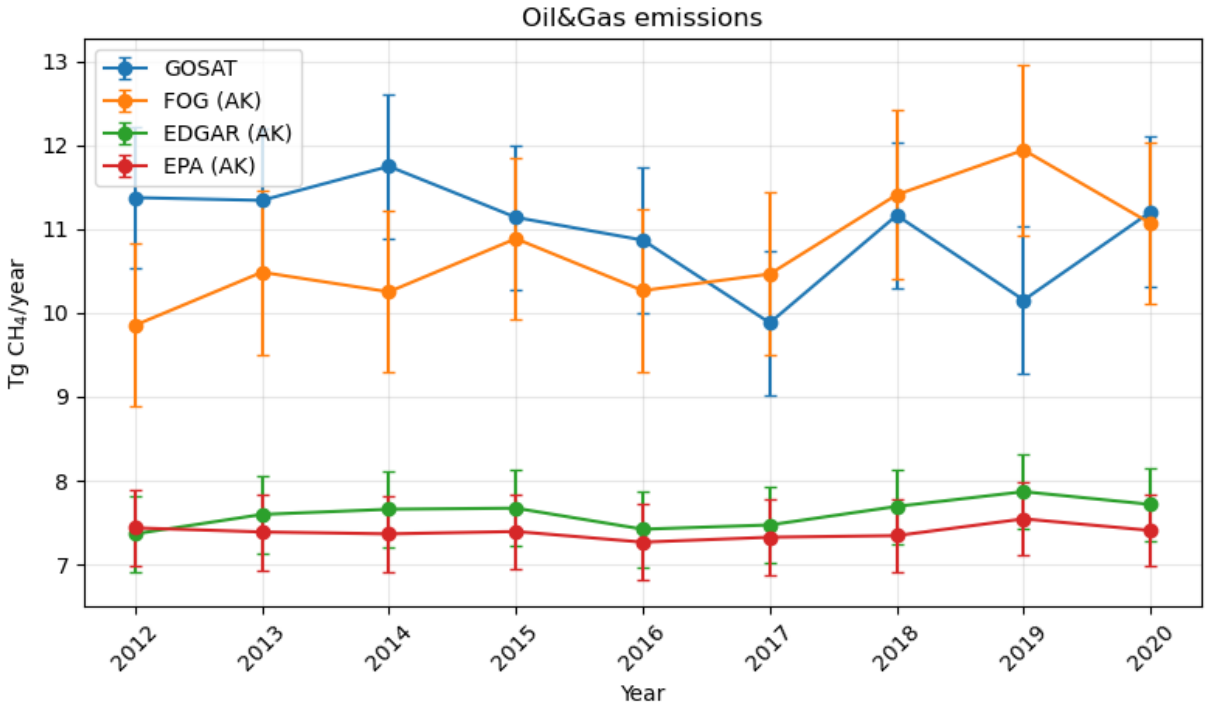

Figure 6: Integrated totals for oil and gas emissions between 2012 and 2020. The GOSAT inversion operator has been applied to the FOG, EPA GHGI , and EDGAR 2024 inventories; the biases between the comparisons are therefore not due to the prior used with the GOSAT inversion.

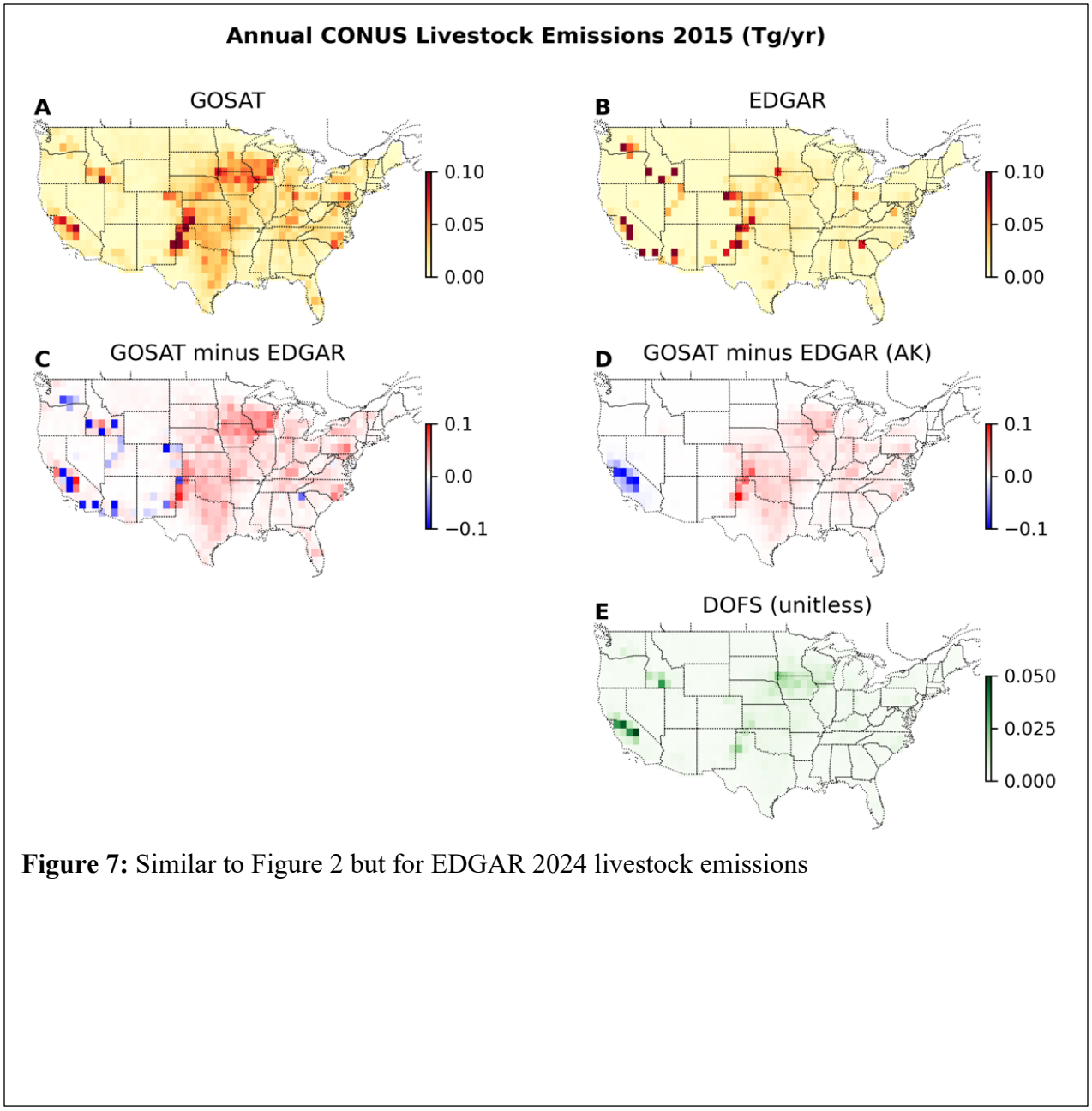

Figure 7: Similar to Figure 2 but for EDGAR 2024 livestock emissions

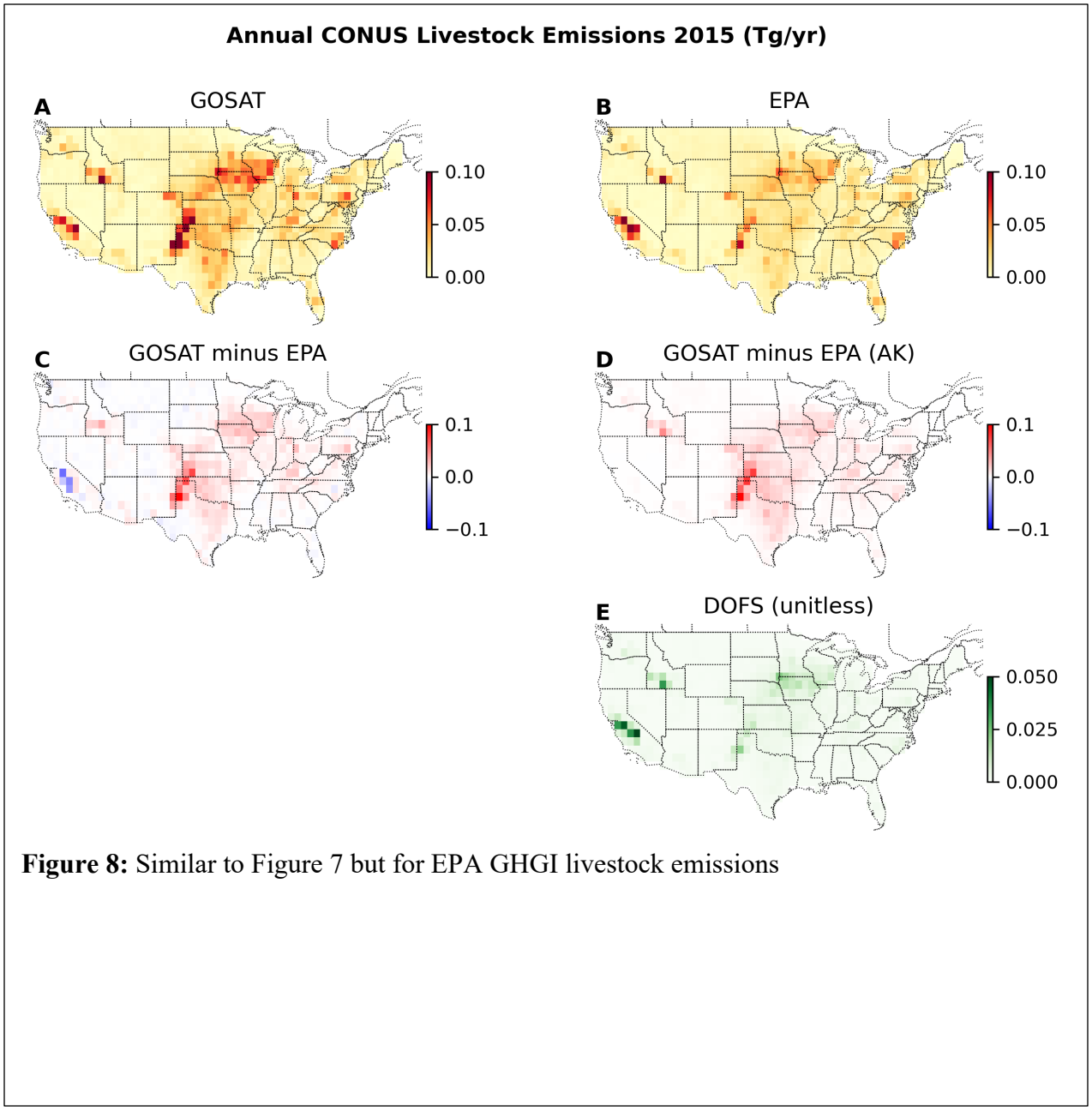

Figure 8: Similar to Figure 7 but for EPA GHGI livestock emissions

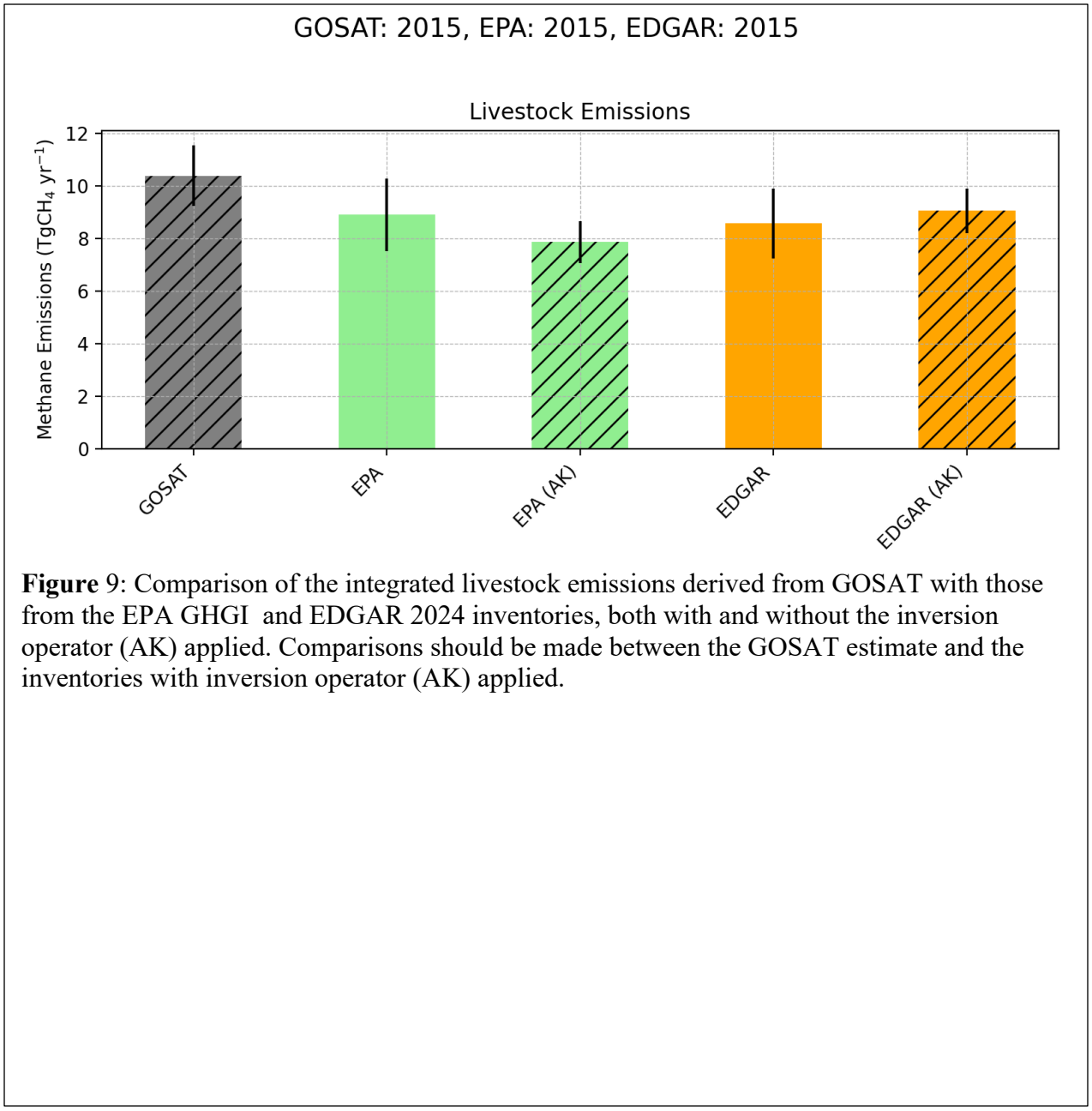

Figure 9: Comparison of the integrated livestock emissions derived from GOSAT with those from the EPA GHGI and EDGAR 2024 inventories, both with and without the inversion operator (AK) applied. Comparisons should be made between the GOSAT estimate and the inventories with inversion operator (AK) applied.

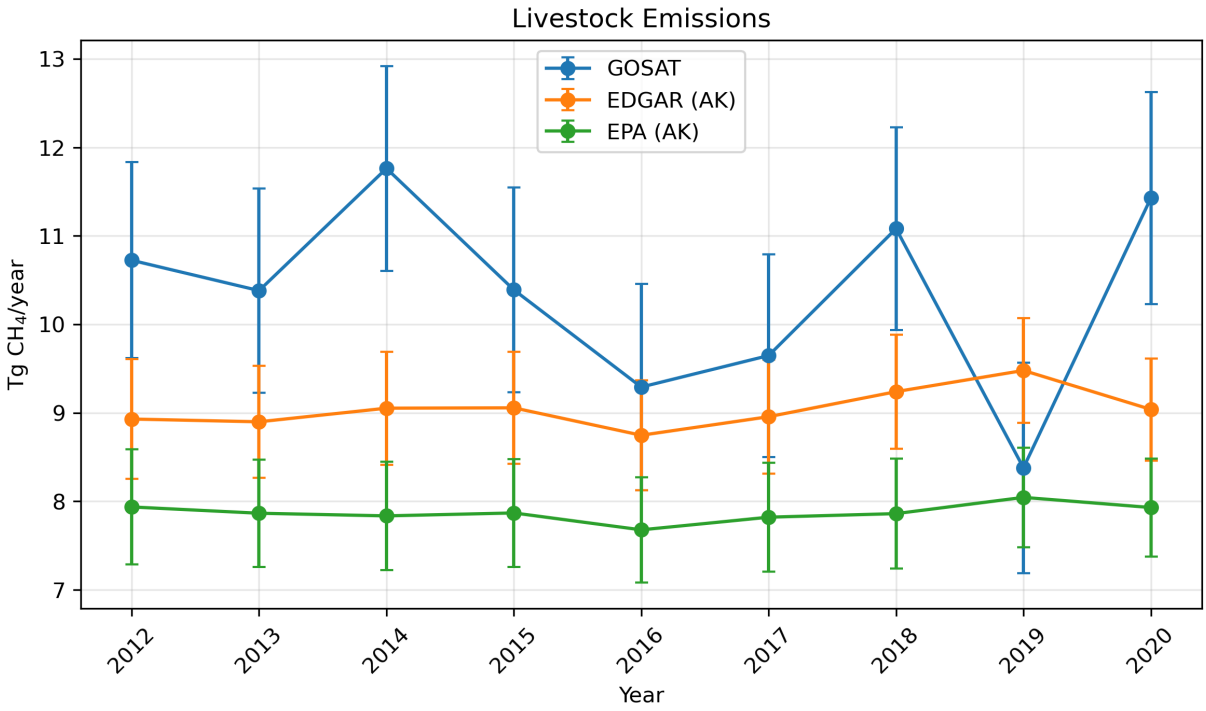

Figure 10: Integrated totals for Livestock Emissions between 2012 and 2020. The inversion operator has been applied to the inventories.

1068

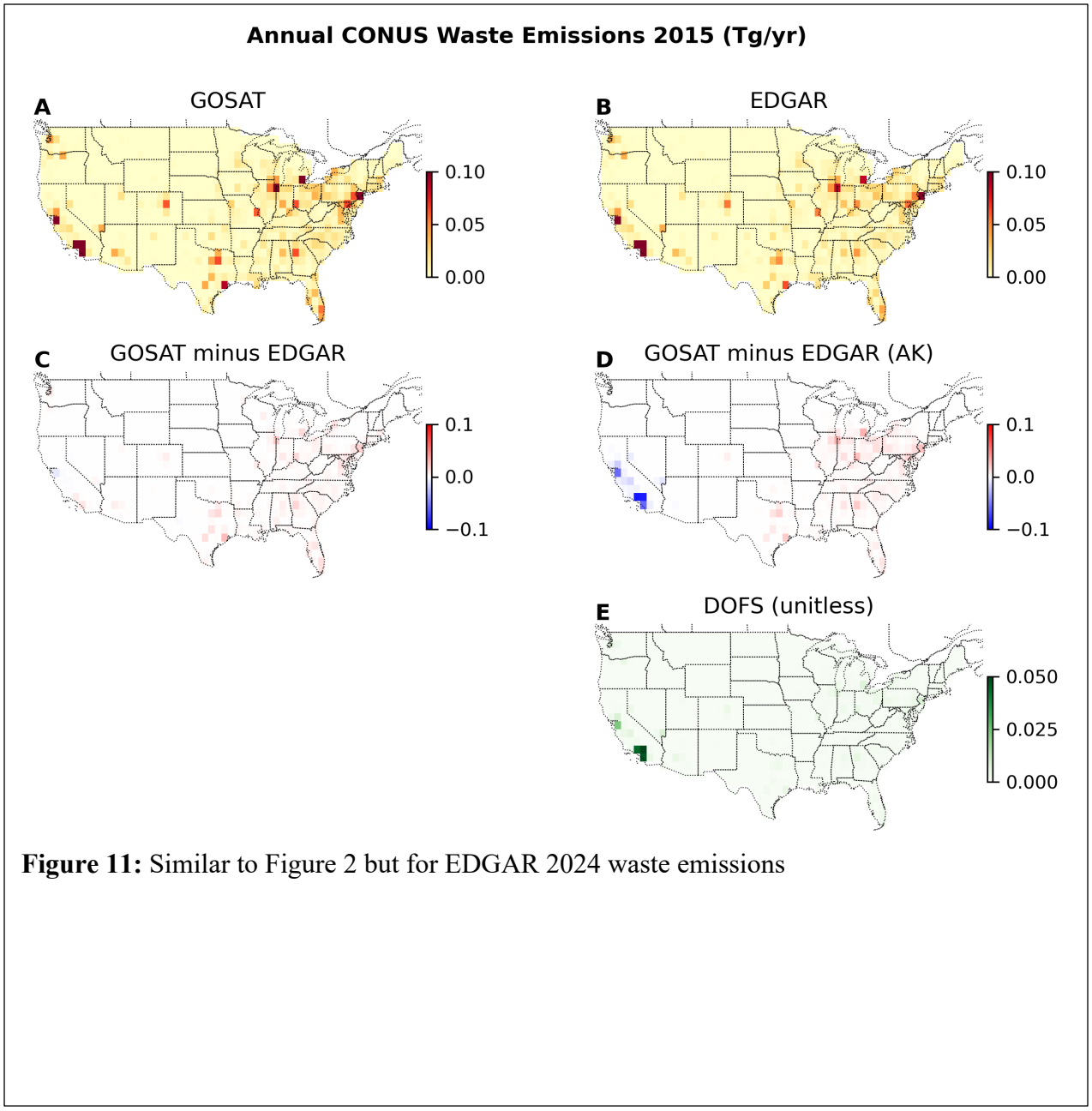

Figure 11: Similar to Figure 2 but for EDGAR 2024 waste emissions

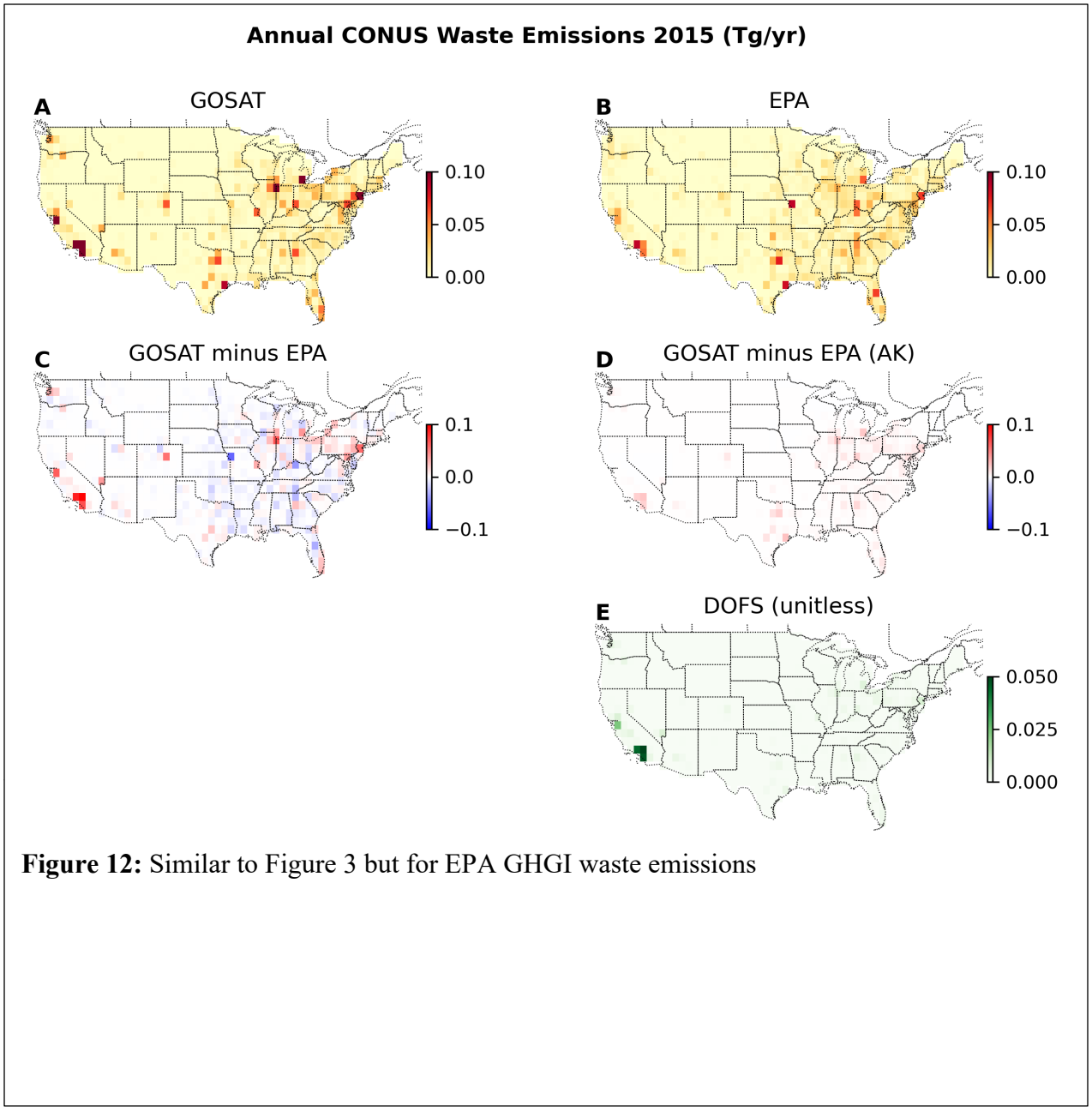

Figure 12: Similar to Figure 3 but for EPA GHGI waste emissions

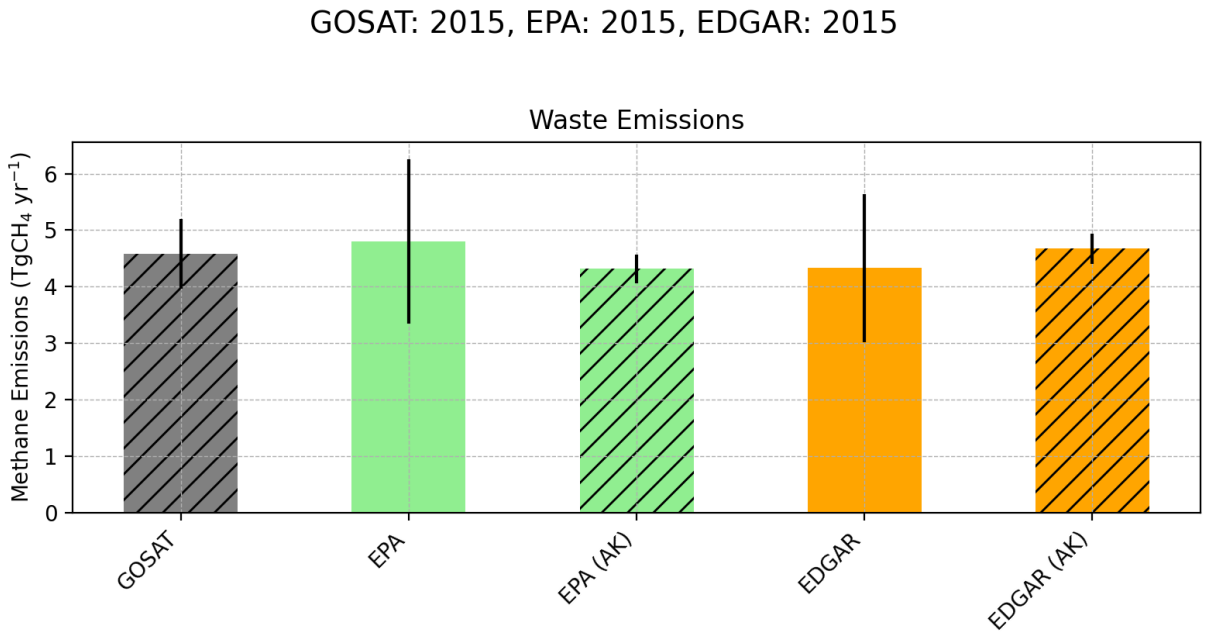

Figure 13: Integrated total methane emissions from the waste sector based on GOSAT, along with estimates from the EPA GHGI and EDGAR 2024 inventories, both with and without the inversion operator applied.

1083